Condensation of the influenza viral fusion peptide alters membrane structure and water permeability

Sourav Haldar[1,4,†], Amy Rice[2,†], Eric Wang[1,2], Paul S. Blank[1], Sergey A. Akimov[3], Timur R. Galimzyanov[3], Richard W. Pastor[2], Joshua Zimmerberg[1*]

[1]Section on Integrative Biophysics, *Eunice Kennedy Shriver* National Institute of Child Health and Human Development, National Institutes of Health, Bethesda, MD 20892, USA.

[2]Laboratory of Computational Biology, National Heart Lung and Blood Institute, National Institutes of Health, Bethesda, MD 20892, USA.

[3]A.N. Frumkin Institute of Physical Chemistry and Electrochemistry, Russian Academy of Sciences, Moscow, 119071, Russia.

[4]Current address: Department of Biochemistry and Bioinformatics, GITAM Institute of Science, GITAM (Deemed to be University), Visakhapatnam 530045, India.

†S.H. and A.R. contributed equally to this work

* Joshua Zimmerberg **Email:** zimmerbj@mail.nih.gov

Keywords
Unilamellar Liposomes, Cholesterol, Membrane Fusion, Influenza, Cell Membrane Permeability.

Running Title:
Condensation of influenza viral fusion peptide

Abstract

To infect, enveloped viruses employ spike protein, spearheaded by its amphipathic fusion peptide (FP), that upon activation extends out beyond a forest of viral spikes to embed into the target cellular membrane. Here we report that isolated FP of influenza virus are membrane active by themselves generating pores in giant unilamellar vesicles and thus potentially explain both influenza virus' hemolytic activity and structure in cryo-electron tomography. Molecular dynamics simulations of asymmetric bilayers with different numbers of FP in one leaflet show substantial peptide clustering. At the center of this peptide condensate a profound change in the membrane structure results in thinning, higher water permeability, and curvature. In effect, a hybrid bilayer forms locally with one lipid monolayer and one peptide monolayer. Membrane elastic theory predicts that the energy landscape becomes favorable for spontaneous pore formation in this novel structure, consistent with the inhibition of pore formation by cholesterol observed experimentally.

Introduction

Cell entry is a crucial process in the viral pathogenic infection cycle. For enveloped viruses, the essence of cell infection is the fusion between viral and host cell membranes allowing delivery of viral nucleic acids into the host cell cytoplasm. For example, influenza virus is endocytosed, whereupon its surface glycoprotein hemagglutinin (HA) encounters a low pH environment. Low pH triggers conformational changes in HA causing exposure of the HA fusion peptide (FP), an amphipathic domain that embeds in the target endosomal membrane [3], while the C-terminal membrane-spanning domain of HA remains embedded in the viral envelope [4,5] at both neutral and low pH. The FP comprises the N-terminal 23 amino acids of HA2, located within the HA ectodomain (at neutral pH), proximal to the HA trimer surface but near its transmembrane domain. This peptide is required for infection in vivo and membrane fusion in vitro, and is featured in all hypotheses on HA-mediated fusion though there is little structural, compositional, or mechanistic data on its exact role [6]. Fusion peptides (FPs) or loops are motifs common in all studied fusogenic glycoproteins from different enveloped viruses, including Zika virus, coronavirus, and HIV. For influenza virus HA, the fusion peptide is a conserved region of the influenza virus genome across many different subtypes of influenza virus [7,8]. Thus, determining its role for infectivity and membrane fusion is critical to finding variant-independent immunogens and pan-viral therapeutics to ameliorate morbidity and mortality.

The influenza FP is required for both intermediates of membrane fusion, hemifusion and fusion pore formation. We recently studied influenza hemifusion intermediates in vitro with high-resolution cryo-electron tomography using a phase plate to enhance signal-to-noise by a factor of four [9]. The cryo-tomograms of influenza viral like particles and receptor-laden liposomes showed the expected 10 nm diameter hemifusion diaphragm in high cholesterol-containing target liposomes, but at lower cholesterol, frequent exposed membrane edges were detected on the target membrane in direct contact with one or more HA still attached at their transmembrane base to the viral envelope; this lipid-protein structure can extend linearly for many nanometers. These surprisingly large ruptures in the membrane *a)* suggest that fusion under these conditions is target-leaky to even large macromolecules and *b)* are consistent with the loss of target liposome contents in studies of intact virus-liposome fusion and a similar cryo-electron tomography study [10,11]. However, it is not known which part of the intact virus or viral like particles create these ruptured target membranes. The purpose of this study is to begin to unravel the physico-chemical

mechanisms by which these exposed membrane edges are formed; specifically, if and how the FP in lipid bilayer poration would initiate such stable edges.

To this end, the single vesicle dye entry assay introduced by Haldar et al. [12] for intact virions was further developed to estimate pore formation by soluble amphipathic peptides in vesicles. We discovered that the HA FP alone was sufficient to cause leakage of dye across lipid bilayers, which we interpret as membrane poration. This HA FP-caused poration was inhibited and its lifetime reduced by cholesterol, as has been seen with activated HA on both viral-like particles and intact, infectious virus. Furthermore, the lipid-dependence of HA FP-induced membrane pores did not require any sterol chemistry but was duplicated by other lipids that promote negative curvature. We conclude that the exposed edges of membrane seen in cryo-tomography were stabilized by FP on the N-terminal end of HA anchored at the viral envelope.

To determine the mechanism by which the HA FP caused membrane poration, the curvature-dependent activity of a FP analog in nanoscale pore formation was probed using a combination of molecular dynamics (MD) simulation and continuum elastic theory. MD simulations were carried out on palmitoyloleoylphosphatidylcholine (POPC) and 1:1 cholesterol:POPC (henceforth chol:POPC) bilayers at increasing FP densities. At low FP density, the predicted positive spontaneous curvature induced by noninteracting FP partially neutralized negative monolayer spontaneous curvature. Using elastic theory, the positive spontaneous curvature generated by the peptide was related to inhibition of pore formation by cholesterol (which has negative spontaneous curvature) in a giant unilamellar vesicle (GUV).

However, a novel structure emerged in the MD simulations at those high FP densities that matched the densely packed hemagglutinin on the virus surface: FP aggregated in the cis leaflet to an extent that lipids were depleted, and the leaflet thinned to almost half its original thickness. Most importantly, the trans leaflet also thinned. The entire novel FP/lipid domain had increased water concentration in the bilayer midplane. Similar behavior is observed at lower peptide concentrations. In each system, the free energy profiles of water beneath the aggregate, in each system, are analyzed using an extension of Marcelja theory [23], indicating a lower energy barrier for pore formation and inhibition of pore formation by cholesterol in accordance with experiment. Hence, two quite different approaches, a traditional one for curvature generation by an isolated "wedge-like" peptide and one explicitly including peptide aggregation, are qualitatively consistent

with the experiments. Distinguishing these models and implications for viral fusion is the subject of the Discussion.

Results

Experimental Results: FP is sufficient to explain cholesterol-dependent lipid pores

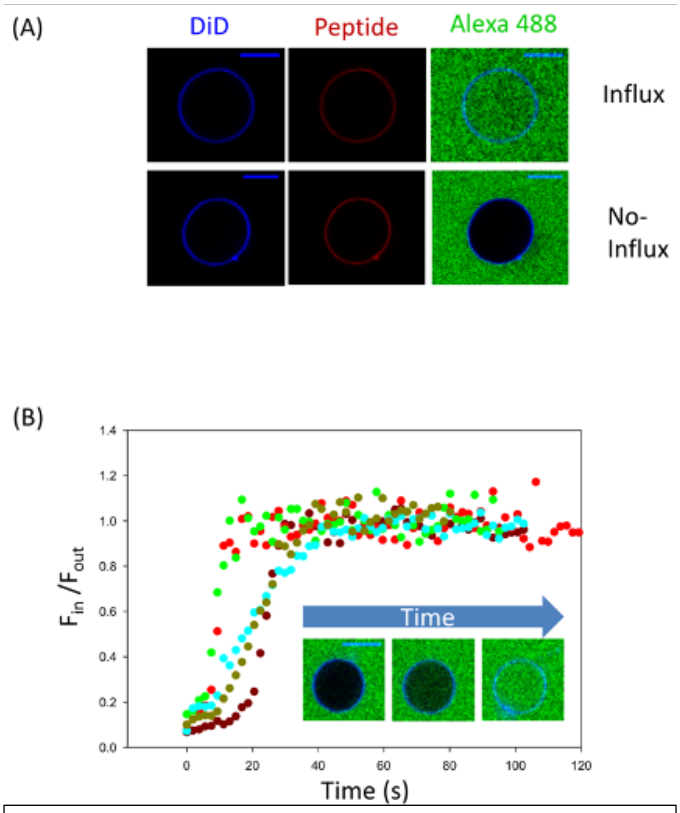

Figure 1. Influenza fusion peptide induced poration of GUV. (A) Representative example of GUVs exhibiting binding of the influenza fusion peptide and influx of Alexa 488 inside GUV as a results of peptide addition or no influx in the presence of peptide. Fusion peptide was introduced from a DMSO stock to a suspension of GUV at a protein to lipid ratio of 1:200. Overall lipid concentration was ~ 0.6 mM. (B) Kinetics of influx following peptide addition. The ratio of average intensity of Alexa 488 in the lumen of GUV with respect to the outside intensity plotted as a function of time. Examples from 5 different experiments (offset in time to the approximate start of leakage) are shown. Inset shows a typical example of vesicle undergoing influx. Scale bars are 10 µm.

Stable pore formation was monitored by confocal microscopy as the influx of water-soluble fluorescent dye Alexa 488 into GUV following FP addition (Figure 1A). Before exposing GUV to peptide, the interiors of the GUV were dark. At neutral pH, FP rapidly bound to POPC GUV upon incubation, and Alexa 488 from the outside media began to accumulate inside the GUV. The intensity of Alexa 488 gradually increased until an equivalent intensity of Alexa 488 was detected inside and outside of the GUV (Figure 1B) -- defined as 100% influx. In the absence of poration, no Alexa 488 influx was detected (Figure 1A lower panel). In two separate experiments, POPC GUV encapsulating 3,000 MW Alexa 488-labeled dextran showed a similar 100% efflux observed as a loss of fluorescence. 100% influx or efflux is consistent with the hypothesis that FP induced pores in POPC GUV are stable on a time scale that allows equilibration of the probe with the external medium and a size large enough to allow transport of both 3,000 and 570.5 MW molecules.

Next, the hypothesis that the probability of detecting FP-induced lipid pores depends upon the lipid composition of the GUV was tested, since viral-induced pores were preferentially detected in target membranes containing low cholesterol (< ~40 mol %) [9,12]. If the membrane destabilizing activity of the intact virus is due to the interaction of the FP with a target membrane, then target membranes comprising higher cholesterol concentrations should increasingly resist FP-induced poration. To test this hypothesis, we incubated POPC GUV prepared from membrane forming solutions of varying cholesterol concentrations (0, 30, and 50 mol %) in the presence of the FP and evaluated the vesicle poration (leakage) fraction. Consistent with our hypothesis, the fraction decreased with increasing cholesterol concentration in the GUV membrane (Figure 2A); leakage probability decreased from around 80% to 40 % for cholesterol concentrations 0 to 50 mol %. Leakage probability was determined roughly 15-18 min after peptide addition to ensure equilibrium. The mean fluorescence intensity within giant unilamellar vesicles (GUVs) did not change after this waiting period.

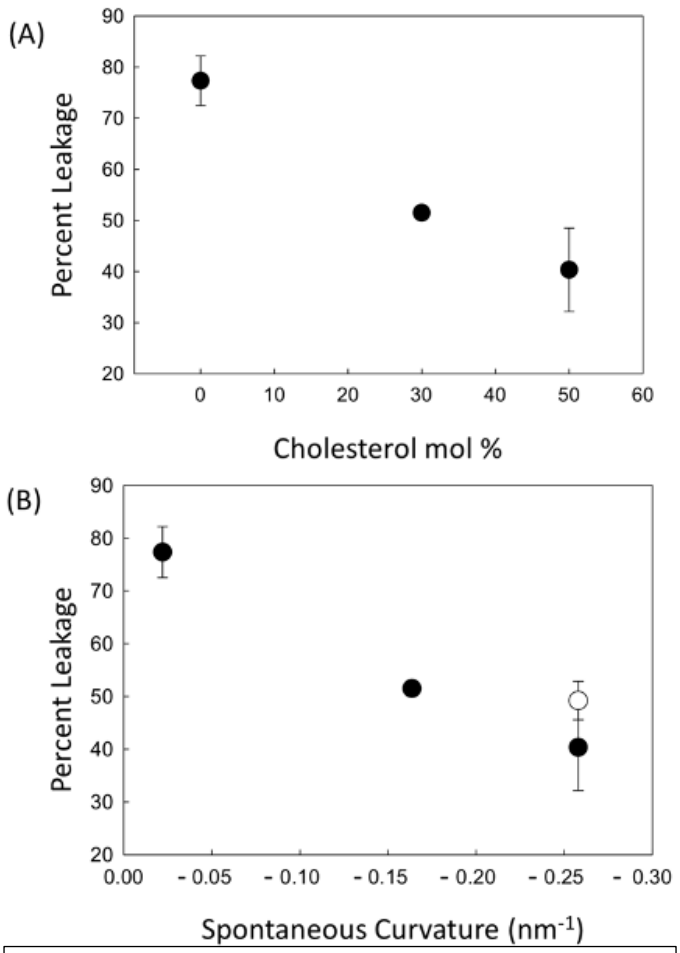

Figure 2. Dependence of fusion peptide induced poration on lipid composition. (A) Degree of poration depends on the cholesterol level in the target membrane. Approximately, 100 vesicles were evaluated for each lipid composition. Error bars represent the SEM of three independent experimental preparations (B) Probability of poration as a function of negative spontaneous curvature of monolayer for cholesterol (closed circles) and for DOG (open circle).

The ring structure of cholesterol confers rigidity to membranes and this property could cause the observed decreasing leakage with increasing cholesterol. To determine whether this effect of cholesterol is due to high negative spontaneous curvature of the GUV monolayer, we

prepared GUVs with the same spontaneous curvature (~ – 0.258 nm^{-1}) as those of the highest cholesterol concentration used in this study (50 mol %), by replacing cholesterol with 24 mol % DOG. The spontaneous curvatures of cholesterol, DOG, and POPC used in the calculations of the mixture spontaneous curvature are: –0.494 nm^{-1}, –0.99 nm^{-1}, and –0.022 nm^{-1}, respectively [13,14]. 24 mol % DOG GUV did not exhibit statistically different poration fractions from 50 % cholesterol GUV (40.3 ± 8.2 % for 50 mol % cholesterol compared to 49.3 ± 4.4 % for 24 mol % DOG; mean ± SEM, n = 3, respectively; p = 0.39, 2-tailed equal variance T-test; Figure 2B); these results are consistent with the hypothesis that leakage and spontaneous curvature are correlated parameters.

We next evaluated whether the pores induced by the FP have similar stability in the presence of cholesterol. To monitor pore stability, we measured the extent of influx, defined as the ratio, $R = F_{in}/F_{out}$, of the fluorescence measured within a GUV (F_{in}) and in the same area outside the GUV (F_{out}), in the presence and absence of 50% cholesterol. The cumulative distribution functions (CDF) of the extent of influx for GUV prepared from pure POPC and POPC with 50% cholesterol are described by generalized Kumaraswamy distributions (CDF = $1 - (1 - z^{\alpha})^{\beta}$; $z = (R - R_{\min})/(1 - R_{\min})$), which are special cases of the generalized beta distribution, with: a) support on the interval [$R_{\min}$, 1]; b) α and β distribution shape parameters, and c) $R_{\min} = 0$ for pure POPC and $R_{\min}$ a fitting parameter for POPC and 50% cholesterol [15,16] (Supplementary Figure 1A). For GUV prepared from pure POPC, $\alpha = 24.0$ (15.1, 32.8) and $\beta = 0.94$ (0.64, 1.24) while in the presence of 50% cholesterol $\alpha = 0.59$ (0.52, 0.66) and $\beta = 1.91$ (1.61, 2.21) with $R_{\min} = 0.065$ (0.063, 0.067) (fitted values (95% lower, upper confidences)); these parameter sets correspond to fractional filling distributional means of 0.96 and 0.26 for POPC in the absence and presence of 50% cholesterol, respectively. Alternatively, since the Kumaraswamy quantile function is $Q(y) = (1 - (1 - y)^{(1/\beta)})^{(1/\alpha)}$, these parameter sets correspond to median quantiles of 0.97 and 0.13 for POPC in the absence and presence of 50% cholesterol, respectively. Pure POPC vesicles exhibited F_{in}/F_{out} ratios close to 1 (> 80%, n = 14 of 17 reported, have filling ratios > 0.95), consistent with influx over a time period sufficient for equilibration with the outside concentration to occur. However, in the presence of cholesterol, vesicles exhibited varying F_{in}/F_{out} ratios ranging from ~0.1 to 0.6 (> 90%, n = 28 of 30 reported, have filling ratios < 0.6). The sub-maximal level of influx in these GUV is consistent with a higher probability of pore closing in the presence of high cholesterol over the time scale of these experiments [17]. This conclusion is supported by remapping fractional filling onto the general kinetic relationship $R = (1 - e^{-t/\tau})$ where τ is a characteristic time constant for the influx process.

Each value of R can now be expressed as an open time, in units of τ, as ($t/\tau = -\ln(1 - R)$). The cumulative distribution functions for the influx time for POPC in the presence and absence of cholesterol are described by generalized exponential distributions (CDF = $(1 - e^{(-\lambda(t/\tau - (t/\tau)_{min}))})^{\alpha}$) with location ($(t/\tau)_{min}$), shape ($\alpha$), and scale ($1/\lambda$) parameters (Figure S1B); this distribution is often used in analyzing lifetime data. For GUV prepared from pure POPC, $\alpha = 17.3$ (4.15, 30.5) and $\lambda = 0.94$ (0.73, 1.16) while in the presence of 50% cholesterol $\alpha = 0.54$ (0.49, 0.60) and $\lambda = 2.25$ (1.92, 2.57) with $(t/\tau)_{min}$ the empirically calculated minima observed, 0.19 and 0.07, respectively (fitted values (95% lower, upper confidences)). From this analysis, we conclude that pure POPC bilayers have a lower probability of closing (> 80% remain open for 3 or more characteristic time constants) than POPC containing 50% cholesterol (> 90% close within 1 characteristic time constant).

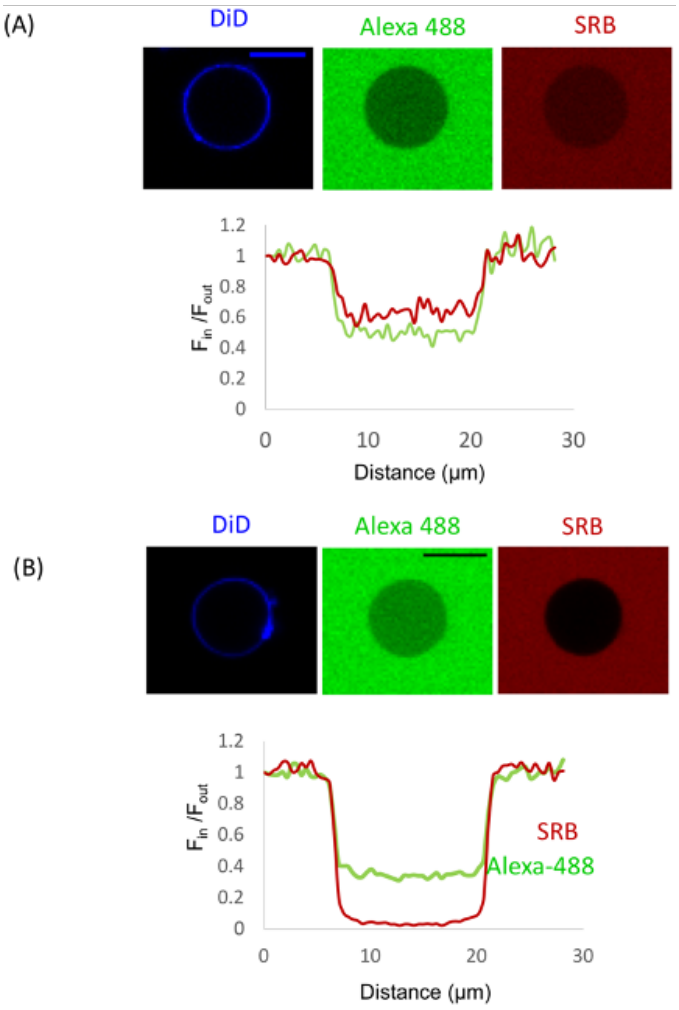

Figure 3. Closure of fusion peptide-induced pores in the presence of cholesterol. (A) Similar degrees of influx were observed when Alexa 488 (green) and SRB (red) were introduced simultaneously. Line profiles of Alexa 488 (green) and SRB (red) quantitatively represent influx. GUVs containing 50 mol % cholesterol were incubated with Alexa 488 and SRB and the fusion peptide was added to the system. (B) Restricted dye entry and exclusion of second dye from vesicles. Fusion peptide was introduced to a suspension of GUVs in the presence of Alexa 488. After 25 min SRB was added to the same suspension of GUVs. Note the differential extent of the influx. Intensity of SRB inside the GUV is negligible compared to Alexa 488. Scale bar is 10 μm.

To further confirm whether submaximal leakage indicates a pore closing event we monitored the influx of a second marker, SRB, introduced after a finite delay following the introduction of the first marker, Alexa 488 [18]. Since SRB and Alexa 488 are of similar molecular weight, if a pore allows entry of Alexa 488 then the same pore should also allow influx of SRB. Consistent with this hypothesis,

when introduced simultaneously, Alexa 488 and SRB show comparable levels of influx (Figure 3A). However, if an initially open pore closes, then the influx of SRB would be restricted. Figure 3B shows the influx of Alexa 488 (the first soluble marker) when incubated in the presence of the peptide, but when SRB was introduced 25 min later to the same suspension, this second soluble marker was excluded, i.e., there was no influx. This result is consistent with the hypothesis that, over this time scale, FP induced pores are not stable in the presence of 50% cholesterol.

HA-induced fusion pore formation is dependent upon the spatial and temporal activity of a critical number of interacting fusion proteins, a configuration consistent with a locally, non-uniform or clustered distributions of fusion peptides. While the spatial resolution of these optical measurements is not sufficient to detect cluster sizes comparable to those modeled using MD (following subsection), departures of the labeled FP intensity on the circular focal slice of the vesicle from a uniform distribution, especially at the time of GUV permeation, support the hypothesis that peptide clustering occurs. Analyses of the distributions of peptide in bulk solution and on the vesicle indicate that, in addition to an increase in the average amount of peptide on the vesicle in time, the variability at the pixel scale (~500 nm^2) also increases in time. Poration occurs with a characteristic time, 101 +/- 22 sec, and peptide density, 2.7 +/- 0.05, (mean +/- SEM; n = 9 including both Alexa 488 and dextran experiments), both log-normally distributed, where the characteristic time represents the difference between the time leakage is first detected and the time the normalized peptide fluorescence on the vesicles increases above the peptide fluorescence in solution (Figure S2 and analyses). The GUV peptide intensity profiles as a function of polar angle are not described by a uniform distribution of fluorophores having a well-defined orientation for either the time averaged profiles or profiles, in time, about the poration event. However, in all experiments, the distribution of pixels for the best fit surface indicated the presence of pixels with larger variance compared to solution; this higher variance is not explained by the differences in intensity suggesting that these higher intensity pixels have higher density and may be the sites of aggregation-induced poration (see Supplementary analyses).

Molecular Dynamics Simulations: individual FP induce positive curvature but aggregate at higher density

Single peptide/leaflet. Figure 4 shows snapshots of POPC and 1:1 chol:POPC bilayers with 1 FP per leaflet (1/1 FP). As found previously for the "boomerang" structure of an influenza FP with a slightly different sequence [19], the neighboring lipids curl under the peptides and keep them well separated from the opposing leaflet (Figure 4). This arrangement allows the peptide to act as a sort of "wedge", inducing positive spontaneous curvature in the leaflet (Table 1). In both the pure POPC and chol:POPC membranes, addition of a single FP to the leaflet makes the spontaneous curvature less negative, indicating that the peptide induces positive spontaneous curvature as hypothesized. This curvature generating effect is stronger in the chol:POPC membrane, where the spontaneous curvature is decreased by a factor of 2. However, because of the strong negative spontaneous curvature of cholesterol, the chol:POPC:FP leaflet is still more negatively spontaneously curved than the pure POPC leaflet.

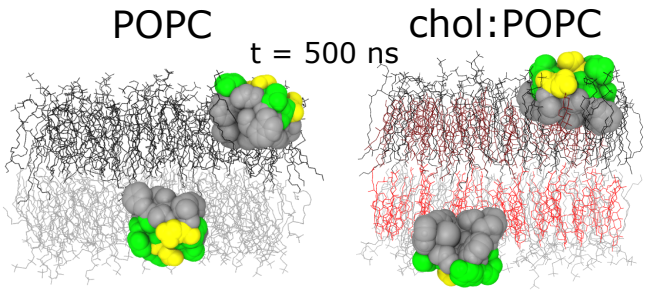

Figure 4. Snapshots of the symmetric (1/1) FP systems. Peptides sit at the hydrophobic/ hydrophilic interface of the membrane leaflet and rarely interact with the opposite leaflet. Lipids in the one leaflet are depicted in darker shades to distinguish them. Hydrophobic residues of the peptide are depicted in grey, while polar residues are green and acidic residues are yellow. Water and ions have been omitted for clarity.

System	R_0 (Å)	C_0 (Å^{-1})	F'(0)	$K_{c,m}$ (kcal/mol)
POPC	−235	−0.0043±0.0008	0.0407±0.0072	9.55[a]
POPC:2FP	−297	−0.0034±0.0013	0.0322±0.0122	9.55[a]
chol:POPC	−58	−0.0173±0.0046	0.2018±0.0542	11.67[b]
chol:POPC:2FP	−129	−0.0078±0.0026	0.0907± .0299	11.67[b]

Table 1. Spontaneous curvature generation by a single FP. The radius of curvature, R_0, is calculated as $1/c_0$. The spontaneous curvature is calculated from *F'*(0), the derivative of the leaflet's free energy with respect to curvature, which is computed from the first moment of the lateral pressure profile. [a] Calculated from bilayer bending constant reported by Venable et al. [1]; [b] Estimated using POPC $K_{c,m}$ and data from Chen and Rand [2]

Concerted action of fusion peptides. To assess how concentration affects the activity of FP, simulations were performed with 1, 6, 10, or 21 FP interacting with the top leaflet of either POPC or chol:POPC membranes (Figure 5). Stable peptide aggregation is observed in both bilayers (Figure 5 and S6-S8); however, peptide clustering is more pronounced in the systems containing cholesterol. The number of peptides in the largest cluster as a function of simulation time for each of the multiple peptide systems are plotted in Figures S6-S8, along with representative snapshots. In all systems where larger peptide clusters formed (n ≥ 5 peptides), these peptide aggregates remain stable on the μs time scale. Interactions between peptides are primarily mediated by direct peptide–peptide hydrogen bonds, rather than water or ion bridges. At first glance, this aggregation is surprising given the net negative charge of these peptides. However, because even a single FP leads to local membrane deformations (see above) resulting in a line tension, clustering of peptides decreases the net line tension of the system which leads to peptide clustering at concentrations above a critical peptide surface ratio $x_0 \sim 0.27$ (see Analytical Theory section below and in the Supplementary text).

These peptide aggregates displace lipids in the upper (cis) leaflet (Figures 5, S9, and S10), and sit much lower in the leaflet than an isolated FP does (Figure S11). This lipid displacement has a profound effect on the membrane – in all systems studied, presence of the FP leads to localized membrane thinning (Figures 6A and S12, and Table S1). In both membranes, this thinning is most pronounced in the 21 FP systems, which have the densest peptide aggregates. The chol:POPC:21FP system thins by roughly 13 Å in the region of the aggregate, while localized thinning in the POPC:21FP system is more moderate 8.5 Å (Figure S12). This combination of thinning and lipid displacement leads to substantial deformation of the trans leaflet (Figure 5 and S13), as the leaflet bows upwards so that the terminal methyl groups of the trans leaflet lipids can contact the hydrophobic underside of the peptide aggregate. Because chol:POPC is much thicker than POPC and displays a greater extend of peptide-generated thinning, the explicit curvature of the trans leaflet is more prominent in these systems.

The displacement of lipids in the cis leaflet by the peptide aggregate, as well as the high degree of thinning of the trans leaflet, suggests that bilayers with FP present would be more susceptible to pore formation. While the conventional MD simulations presented above are not of sufficient length to generate pores or even pre-pore configurations such as water wires, they do yield information on water content. The probability distribution of water in each membrane

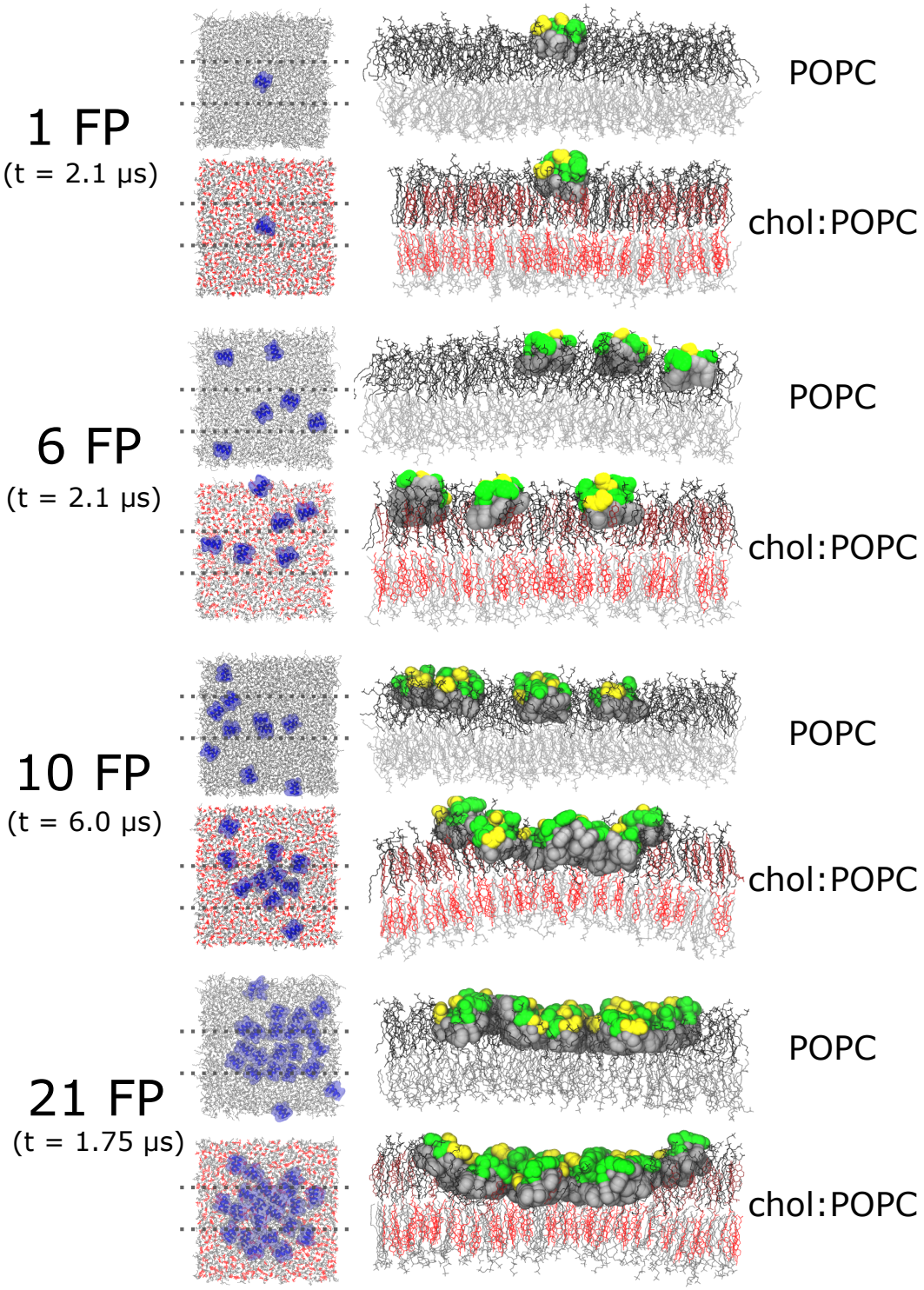

Figure 5. Snapshots of microsecond time-scale MD simulations. Final simulation snapshots. POPC and cholesterol are shown in grey and red line representations; peptides are depicted as blue-ribbon diagrams with a translucent space-filling overlay in the top-down views. Side view of the final simulation snapshots are taken as a 40 Å section denoted by the dotted lines in the top-down views; lipids in the cis leaflet are depicted in darker shades to distinguish them. Peptides are depicted in a space-filling representation, with hydrophobic residues in grey, while polar residues are green and acidic residues are yellow.

can be related to R, the resistance to permeability, by the inhomogeneous solubility diffusion (ISD) model (Eq. 3 Methods) [20]. These relative resistances to permeabilities can be taken as measure of the propensity of these bilayers to porate.

The free energies, $F(z)$, for water (Eq. 2 in Methods) in the peptide-containing and peptide-free POPC and chol:POPC bilayer systems are plotted in Figure 7. All systems show low free energy in the well-hydrated headgroup region and a substantial free energy barrier in the hydrophobic hydrocarbon region. The barrier at the midplane (z=0) for pure POPC is characteristic of most homogenous bilayers [21]; the metastable minimum at the midplane in chol:POPC results from chain ordering and is found in liquid ordered phases [22]. Addition of a single fusion peptide only slightly lowers the free energy barrier, while the large aggregates observed in the 21 FP simulations substantial alter the energy landscape. The barrier height is reduced by approximately 1 kcal/mol for POPC:21FP, and the width at half-height by roughly 4 Å; the barrier height is relatively unchanged for chol:POPC:21FP but the width at half-height is reduced by 15 Å. Furthermore, the plateau region characteristic of cholesterol-containing membranes is absent in both the 21 and 10 FP systems. Aggregates of intermediate sizes (6 and 10) have modulated effects following the same trend as the extreme cases of 21 FP and peptide-free – reduction of the barrier height and concomitant narrowing in the POPC membranes, and narrowing with an associated shape change in chol:POPC.

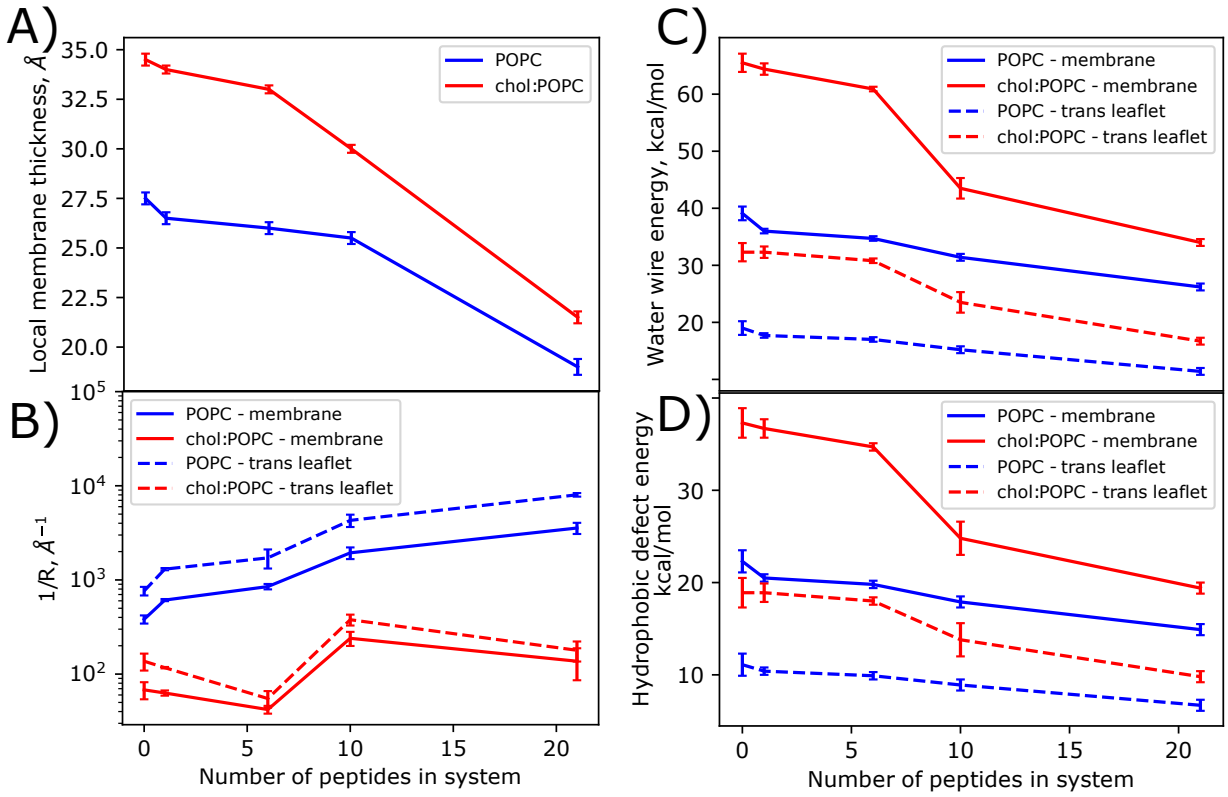

Figure 6. Thickness, resistance, and pore energetics for all systems studied. Data for all four plots is given in Tables S1 and S2. A) Local hydrophobic thickness of the POPC and chol:POPC membrane with varying numbers of FP present. B) Values of inverse resistances to water permeability, 1/R, for both membranes with varying numbers of peptides present. C) Energy of water wire formation in POPC and chol:POPC membranes in the absence and presence of FP. D) Energy of hydrophobic defect in POPC and chol:POPC membranes. Error bars in panels C and D have been multiplied by 2 for clarity. Lines joining the data points are viewing guides.

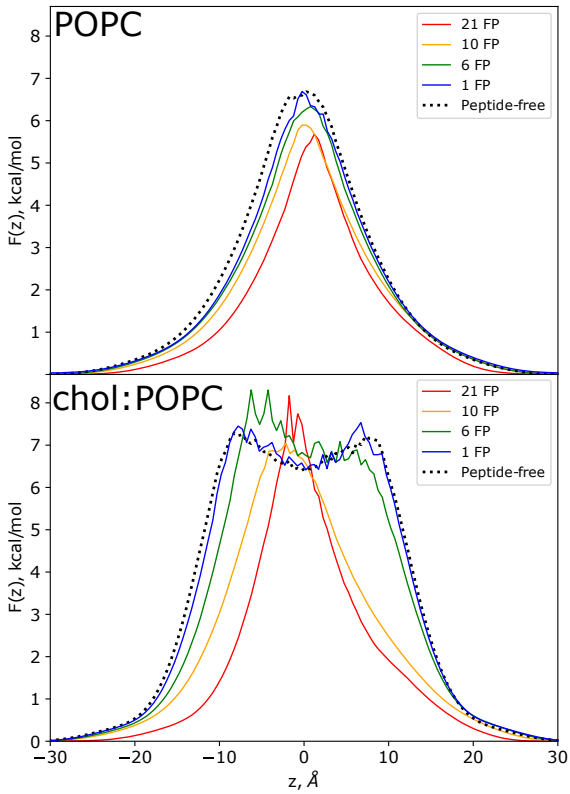

Figure 7. Free energy $F(z)$ for water as a function of position along the membrane normal. Free energy profiles for pure POPC systems are shown in the top panel, while 1:1 chol:POPC systems are in the bottom panel. Solid, colored lines are systems with fusion peptide present in the top leaflet, while the dotted black lines are data from the peptide-free systems. Data calculated only for water molecules within a cylinder of radius 30 Å and centered at the origin (depicted in Figure S14).

The resistances to water permeability evaluated from $F(z)$ and the ISD model are provided in Figure 6B and Table S2, along with the energies of water wire and hydrophobic defect formation calculated in the following subsection. Since the permeability P is proportional to $1/\bar{R}$, it is most instructive to compare values of $1/\bar{R}$ between systems. The change when adding peptide aggregates is substantial for POPC – a 9-fold increase in $1/\bar{R}$ for the 21 FP case – while the 21 FP aggregate has a more moderate 2-fold increase for the chol:POPC membrane. Most notably, $1/\bar{R}$ for POPC:21FP is 26-fold larger than for chol:POPC:21FP, implying that the permeability to water is lower by a factor of 25 when cholesterol is present. Even the presence of a single FP increases this ratio from ~5 to 10, indicating a stronger effect on the pure POPC membrane. In all, these simulations at varying FP concentrations show that the activity of multiple FPs is distinctly cooperative and fundamentally different from that of an isolated peptide – FP aggregates thin the membrane and increase its permeability in a concentration-dependent manner.

Electroporation simulations. Pores can be formed readily by an applied electric field. While simulations with a field are not directly relevant to the present experimental system (where pores formed without an applied field), they do provide some insight to the sequence of poration stages

and the differences between the bilayers with and without cholesterol. Selected results from a series of simulations with an applied electric field, presented in the Supplementary Materials, show that pores form more readily in POPC:21FP systems than in chol:POPC:21FP (as shown in experiment and predicted by the conventional MD simulations). The formed pores follow the sequence: water wire, hydrophobic pore, hydrophilic pore, in agreement with theory [23].

Analytical Theory

General Considerations. Dye leakage following peptide addition is consistent with the formation of peptide induced pores in the membrane. Pore formation, followed by irreversible membrane rupture, is at least a two-stage process (Figure 8). First, a hydrophobic pre-pore appears. The pre-pore growth and its conversion to a hydrophilic pore require surmounting an activation barrier, the peak of which is estimated to be located at a critical pore diameter of about 1.3 nm (see Figure 8). As a result, a metastable hydrophilic pore of minimal luminal radius is formed. Widening of this hydrophilic pore leads to irreversible rupture of the membrane under external tension and requires surmounting a second energy barrier. Thus, there are two energy barriers on the way to irreversible membrane rupture. As membrane rupture was not observed experimentally (GUV resealed in ~20 min.), we conclude that the second energy barrier was never crossed. Thus, we attribute leakage to the metastable hydrophilic pore and focus on the first activation barrier, at a pore diameter of ~1.3 nm. At the top of this barrier, the energies of the hydrophobic defect and hydrophilic pore match; thus, the barrier can be estimated as the energy of this critical hydrophobic defect. To analyze the

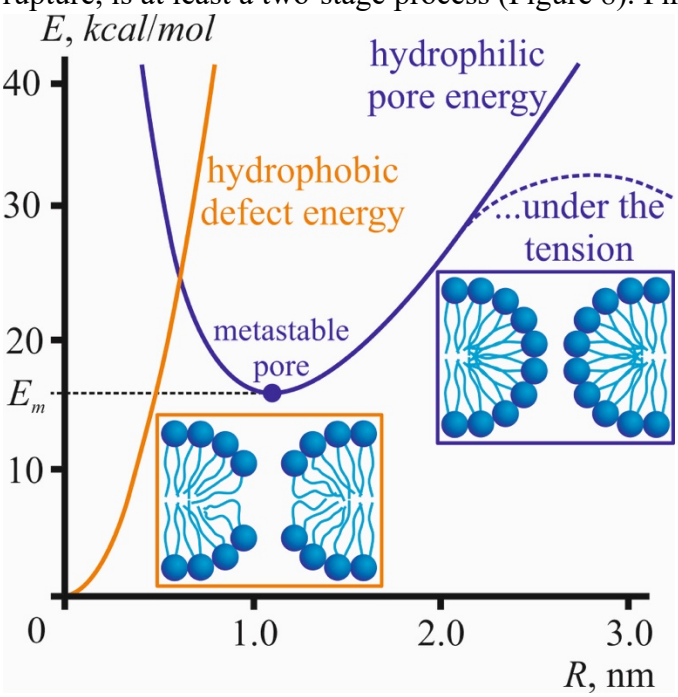

Figure 8. A typical pore energy profile. The orange curve corresponds to the total energy of the hydrophobic pore (sketched in the orange box), and the dark blue curve corresponds to the elastic energy of the hydrophilic pore; the dashed blue curve corresponds to the case of applied lateral tension. The cartoon in the dark blue box represents a metastable hydrophilic pore of energy E_m.

system investigated in the experiments and MD simulations, we utilized a theory combining the Helfrich theory of elasticity of lipid membranes [24], an approach to describe interactions of hydrophobic surfaces with water [25], and a model for the peptide microdomain. These continuum theories have shown their effectiveness in describing various membrane processes accompanied by a change of membrane topology, such as fusion [26,27], fission [28], and poration of single-component lipid membranes [23,29,30]. As a FP cluster was formed in the MD simulations, consistent with experimental observations, we analyzed the conditions for formation of this cluster. As presented in the SI, the energy difference of the systems of clustered and dispersed FPs was shown to depend on FP concentration and the size of the clusters. Upon exceeding some critical concentration of FP on the membrane, the formation of a metastable cluster became favorable as compared to FP dispersion, while at lower concentrations the cluster was predicted not to form (Figure S18). The details of these calculations are presented in the Supplementary Material.

Isolated peptides. At subcritical concentrations, the FPs are predicted to be randomly dispersed in the membrane. In the framework of the developed theoretical model, in this dispersed case the FPs are considered as membrane components that modify the average elastic modulus and spontaneous curvature of the corresponding lipid monolayer.

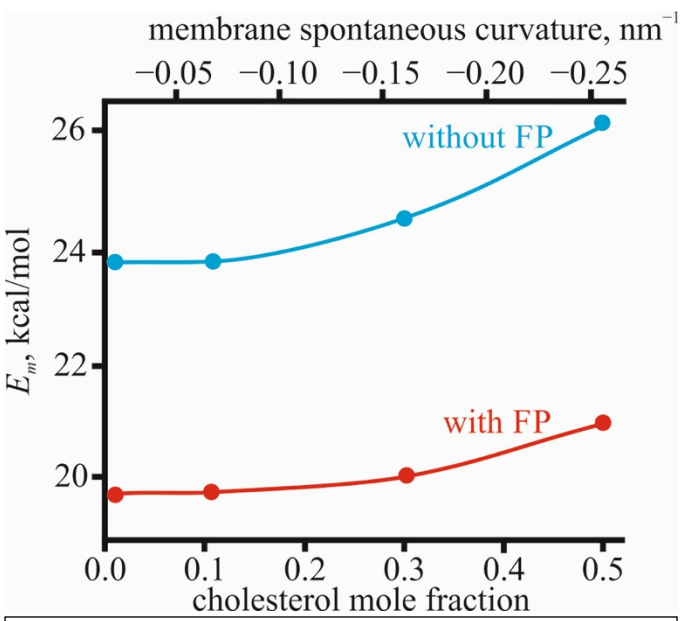

Figure 9. The dependence of the energy of the metastable pore on the cholesterol concentration (monolayer spontaneous curvature in the upper scale) in the absence (blue) and presence (red) of FP. The energy was calculated at the indicated mole fractions (red and blue circles); the solid curves were drawn as a visual guide.

Figure 9 illustrates the dependence of the energy of the metastable pore on the cholesterol concentration (lower scale) and monolayer spontaneous curvature (upper scale). The pore energy increases by about 2.4 kcal/mol = 4 k_BT when the cholesterol concentration increases from 0 to 50%, thus leading to hindrance of pore formation and destabilization of opened pores (k_BT ~ $4.14 \cdot 10^{-21}$ J at room temperature, T = 300

K). Addition of FPs drops the pore energy by about 5.6 kcal/mol = 7 k_BT, thus promoting pore formation. In the absence of FPs, the pore energy is too high to be supplied by thermal fluctuations.

Multiple peptides. The concentration in the MD simulation systems of 21 FP per monolayer was slightly supercritical, and under the simulation conditions the predicted size of the metastable cluster was like that observed in the MD simulations (Figure S19).

The energy of the hydrophobic defect in both homogeneous (purely lipidic) and inhomogeneous (with adsorbed FP) membranes can be estimated from the water PMF data obtained by MD simulations (Figure 7). First, we calculate the energy of the water-wire, assuming that the energy of each water molecule in the wire is given by the PMF energy profile $\varepsilon(z)$:

$$W_{wire} = \frac{1}{3\,\text{Å}} \int_{box_{\min}}^{box_{\min}} \varepsilon(z)\,dz \qquad (1)$$

where 3 Å is the "length" of the water molecule, and box_{min} and box_{max} are coordinates of the simulation box boundaries along the z-axis. Corresponding energies are summarized in Figure 6C and Table S2. However, this procedure overestimates the energy of the water-wire and hydrophobic defect, since water molecules in the wire form favorable hydrogen bonds with their neighbors, while the PMF profile was obtained for separate water molecules, which had no such opportunity. Therefore, we have normalized the values W_{wire} by the energy of a water-filled cylinder E_H of the critical diameter ~1.3 nm in the hydrophobic media calculated using Marčelja theory [23,25,30], taking the pure POPC membrane as a reference system. These calculated values are plotted in Figure 6D and listed in Table S2. FPs drop the first energy barrier by 30%, from ~22 kcal/mol to 15 kcal/mol for the case of pure POPC, and by half for the case of the chol:POPC system (from ~37 kcal/mol to ~19 kcal/mol). Cholesterol increases the barrier height by ~70% in the peptide-free membrane and by ~25% in the presence of FPs.

The calculated shape of the membrane without the hydrophobic defect is presented in Figure S20A, top; it qualitatively agrees with the membrane shape observed in the MD simulations. The shape of the membrane with a 1.3 nm diameter hydrophobic defect is presented in Figure S20A, bottom. To analyze the effect of a FP cluster on pore formation, we calculated the dependence of the energy of the hydrophobic defect in the center of the FP cluster on the cluster size (Figure S20B). We have found that the cluster facilitates formation of a hydrophobic defect. In the presence of the cluster, the energy of the hydrophobic defect decreases (Figure S20B)

because the "hybrid" FP/lipid bilayer is thinner than the pure lipid bilayer. The energy of the hydrophobic defect is ~ 2.4 kcal/mole = 4 k_BT smaller in the large (e.g., 10 nm radius) cluster as compared to the case of a purely lipidic bilayer. There is an optimal cluster size (3 nm radius) where the energy of the hydrophobic defect is 4.8 kcal/mole = 8 k_BT smaller than in the purely lipidic bilayer, and 2.4 kcal/mole = 4 k_BT smaller than in the large cluster. This difference in energy leads to a Boltzmann factor $e^{-4} \sim 0.018$ corresponding to about 50-fold increase in probability of hydrophobic defect formation in a cluster of the optimal size as compared to the large cluster.

The predicted energy effect of FPs on poration is weaker when FPs are postulated to modify only the membrane elastic parameters, as compared to predicted energies that consider FP cluster sizes and utilize water PMF measurements. This may point to the importance of accounting for collective protein-protein and protein-lipid phenomena in the description of the poration process.

Discussion

The genomes of most enveloped viruses enter their target cells via the endocytic pathway, where the viral envelope spike protein encounters acidic pH. Rosette formation was one of the first electron microscopy visualizations of purified viral spike proteins from rabies, rubella, influenza, and other viruses. [31-38] For the influenza virus spike protein hemagglutinin, its low pH activation is necessary and sufficient for triggering the fusion of virus to target membrane, including receptor-doped phospholipid bilayers. While activation of virus or isolated trimers bound to red blood cells led to hemolysis, in the absence target membrane, activation of isolated soluble ectodomain led to new rosettes of those trimers [31,32]. The N-terminal domain of HA proved responsible for this aggregation of HA ectodomains seen as a rosette; this short peptide is now known as the fusion peptide (FP). Since the FP is amphipathic, rosette formation was considered a consequence of the hydrophobic effect: the hydrophobic surface formed by one side of the FP would avoid water via self-aggregation. Here, in a study of the membrane mechanisms by which influenza virus can disrupt its target membrane (as in hemolysis) we establish the FP to underly this disruption -- in target membranes, a reversible pore forms upon addition of FP in the absence of virus or even the rest of HA (Figure 3). Furthermore, in MD simulations crafted to understand the chemistry by which FP generate sufficient curvature stress to porate the usually stable lipid bilayer, a new phenomenon emerged: the aggregation of FP via their lateral side chains into FP microdomains (Figure 5) that had the power to locally thin (Fig 6A) and curve the bilayer, and significantly increase the probability of water entry (Figure 7) and permeability (Fig 6B). Continuum elasticity theory estimates that the barriers for pre-pore states (water wires and hydrophobic defects) are lowered as peptide concentration increases and aggregation ensues (Fig 6, Table S2), thereby accelerating pore formation compared to bilayers with non-interacting FP. Lateral self-aggregation of amphipathic helices, crucial to many membrane, regulatory, and remodeling proteins, may be a general motif in bio-membrane systems, and may represent an evolved instance of the nucleation event for cytoplasmic protein condensation [39].

Disruption of lipid bilayers by the influenza FP in experiments and simulations

Bulk spectroscopic measurements have shown FP leading to release of contents from large unilamellar vesicles (LUVs) composed of soybean azolectin, egg PC, and PS/PC (1:1) [31-40],

consistent with subsequent electrophysiologic recordings of planar phospholipid bilayer membranes [10], and electron and light microscopy [9,12]. These studies agree that the stability of the target membrane is compromised under conditions promoting fusion between bilayer membranes and influenza viruses or influenza viral-like particles (VLP). While these findings indicated that the influenza FP and its analogs destabilize the membrane, they did not show whether these permeability changes are associated with stable pores. Here, in single FP-GUV experiments, fluorescent dye influx continued over minutes, suggesting that the FP-induced influx does not proceed via a short lived transient flickering pore but rather via either a stable or constantly flickering pore [18]. The lipid dependence by which FP induce stable pore formation at neutral pH was the same as determined in the previous studies on intact virion and VLP.

Molecular dynamics simulations have previously demonstrated the ability of isolated FP to distort the bilayer,[41] and more recent simulations[42] related such distortions to positive curvature generation, so the observation from these simulations that a single FP per leaflet (1/1 FP) generates positive spontaneous curvature (Table 1) is perhaps not surprising. These simulation results are consistent with several studies describing the interaction between the FP and model membranes. For example, x-ray diffraction and differential scanning calorimetry indicate that the FP induces curvature stress that destabilizes DiDOPE membranes [43,44]. In the low-density regime, FP are considered as membrane components modifying the elastic parameters of the corresponding lipid monolayer. Thus, we conclude that isolated fusion peptides generate positive spontaneous monolayer curvature. It is possible that the positive spontaneous curvature induced by isolated FP could facilitate formation of metastable pores in POPC membranes, and partially compensate the effect of hindered pore formation arising from negative spontaneous curvature of cholesterol in the chol:POPC membrane[23]. DOG-containing vesicles with the same negative spontaneous curvature as cholesterol-containing ones exhibited a similar inhibition of the degree of poration (Figure 2), suggesting that it is not the chemical structure of cholesterol *per se* that is responsible for cholesterol's pore neutralization activity.

At higher densities, FP aggregate

MD simulations at higher density (6/0, 10/0, and 21/0 FP) were motivated by the observation that hemagglutinin is densely packed on the virus surface. Specifically, the

approximately 9.5 nm spacing [9,45] implies that the centers of 7 HA forming a centered hexagon can be contained in a square patch of 15.3 nm/side. Since there are 3 FP per HA, in principle 21 FP could maximally fit in such a patch. The 15 × 15 nm^2 surface areas of the 21/0 FP bilayers thus model the upper limit of surface density of FP on a cell surface. MD simulations of spontaneously emerging aggregates of FP on a single leaflet yielded qualitatively different results from those obtained at infinite dilution. Now the FP aggregated and displaced many lipids in the cis (top) leaflet, thereby thinning that leaflet. Whereas a *single* FP coexists with a large ensemble of lipid configurations featuring tails that can spread under the FP, lipid tails adjacent to the peptide *aggregate* were only partially able to shield the hydrophobic underside of that aggregate. Furthermore, at the highest FP densities (21/0 FP) the *trans* leaflet thins and becomes negatively curved (concave) as the terminal methyl groups interact with the remaining exposed regions of the aggregate's hydrophobic underside (Figure 5). This curved region of the membrane is more permeable to water, as evidenced by the substantial changes to the water PMF in the region of the peptide aggregate.

Pores were not formed in any of the simulations (without adding electrical fields, see Supplementary Material), likely due to an energy barrier incompatible with the short atomistic simulation durations currently practical. Consequently, analytic theory had to be constructed to bridge the gap between simulation and experiments. Because the underlying ultrastructure of a FP membrane microdomain is radically different from that of a fluid mosaic FP-embedded bilayer, lipid monolayer elastic theory was inappropriate under conditions where lipid-protein interactions dominate the physics. In the high-density regime, theoretical considerations predicted a critical FP density on the membrane, beyond which FP aggregate (Figure S18). Furthermore, the hybrid bilayer (one FP rich monolayer, one lipid monolayer) was analyzed by a theoretical treatment based on the Hamm & Kozlov[46] formalism, hydration of hydrophobic surfaces, and the FP microdomain. Compared to previous estimates of the lowest energy pathway in lipid bilayers composed of longer chain lipids, the FP hybrid had an even lower energy pathway to membrane poration[30,47-50]. Moreover, it is predicted that pores form most readily at an aggregate radius of 3 nm (Figure S20). This optimal aggregate size is in principle achievable at physiological HA density. Illya and Deserno observed qualitatively similar aggregation in their simulations of highly

coarse grained peptide/bilayer systems [51], and coarse grained methods should be useful for further studying aggregation of these fusion peptides.

A theoretical mechanism for leaky fusion[10] has been proposed where the stalk destabilizes the membrane in its vicinity leading to pore formation in one or both merging bilayers [52-54]. Schick (2011)[55] reported that, in turn, the stalk is predominantly formed in the stressed regions of the membrane, e.g., in the vicinity of the pore or FP aggregate boundary. If the FP promotes formation of the pore and, consequently, of the stalk then a linearly expanding stalk may encircle the pore and transform to the fusion pore thus completing merger of membranes, similar to the "stalk-hole complex" mechanism proposed in Katsov, Müller, & Schick (2006)[54].

Which approach, isolated peptide or aggregate, provides the better description to the experimental poration results reported here? Firstly, the quantitative treatment of independent peptides as modifiers of the elastic parameters of the membrane yields too small a difference of metastable pore energy when comparing the chol:POPC membrane subjected to FP and the pure POPC membrane without FP; see Figure 9, right-most point of red curve and left-most point of blue curve. In this comparison, this small difference means that pure POPC membranes should spontaneously perforate. But that prediction is not borne out by the experimental observations. Secondly, the finite time of GUV leakage (Figure 3) is better explained by the aggregate model of peptide action. Aggregate formation requires that the density of FPs exceed the critical density. Upon pore formation, the peptides can flow to the opposite monolayer of the membrane, thus reducing the concentration of FP in the cis monolayer below the critical value. If FPs serve only to modify the monolayer spontaneous curvature, the probability of pore formation should depend on the total amount of adsorbed FPs on the membrane; nothing changes upon formation of the pore and there is no reason for pore closure. Furthermore, the theoretical energies of water wire and hydrophobic defect formation are also considerably lowered in the aggregated FP-containing systems. Since pore formation is believed to progress through water wires which expand first into hydrophobic pores[23], we expect pores to form much more readily in these systems.

In all, the simulation results demonstrate an unmistakable difference between the action of a single FP and an aggregate. MD data provide guides for calibration of hydrophobic defect energies that allow a generalization of continuum theory to analyze hydrophobic defects formed

in asymmetric membranes, e.g., in the center of an FP cluster facing a pure lipidic monolayer. This expansion provided estimates of energy barriers of pore formation in membranes with complex compositions. The calculations demonstrated an increase of the energy barrier in the presence of cholesterol and abrupt reduction of the barriers by FPs, both in isolated and cluster-forming configurations.

How are cells infected: fusion or pores?

The cholesterol-inhibited poration shown here is a likely explanation for the membrane-edge stabilizing activity seen in low cholesterol under conditions promoting viral-vesicle fusion entry [9,12]. It is hard to imagine that the FP and the transmembrane domain (TMD) cooperate as the essential pore-forming components of the fusion pore that initiates membrane fusion, even though mutations in the FP or deletion of the TMD can independently practically nullify fusion pore formation [56]. However, in the canonical stalk-pore fusion pathway, neither the FP nor the TMD can access the hemifusion diaphragm (HD) by diffusion either in the aqueous or the hydrophobic space. Furthermore, while increased cholesterol in the target membrane *inhibits* FP-induced pores, increased cholesterol in the target cell *promotes* fusion pore formation leading to influenza virus infection [57] and reduces the flickering pore transit time [58]. If an underlying evolved activity of the highly conserved FP is to aggregate, as seen in this study and in rosette formation, and cholesterol inhibits in the hybrid FP microdomain, we conjecture that the work done by the FP microdomain comes later in the fusion process, after HD formation, when it would coat the monolayer trans to the HD. There it may induce a *bone-fide* fusion pore at the edge of the HD. In support of this notion, protein domain insertion at a distance (into a monolayer trans to the remodeling monolayer) plays a critical role in lowering the activation barrier for fusion in two other membrane remodeling systems: PH domain insertion in dynamin-mediated membrane fission [28,59] and cell-cell fusion where myomaker acts after myomerger to form the fusion pore [60,61]. In both systems, the protein domain action is thought to occur near or at a three-way lipidic junction [59,60]. It remains for future work to perform MD of FP on the three-way junction to determine if FP aggregation can proceed in that geometry and if cholesterol promotes pore formation at a distance from the FP in the HD. Finally, we cannot exclude the possibility that entry of intact enveloped virion through ruptured endosomes is sufficient for cell infection, via subsequent envelope disruption and intracellular trafficking to the nucleus.

Materials and Methods

Materials

1-palmitoyl-2-oleoyl-*sn*-glycero-3-phosphocholine (POPC), cholesterol, and 1-2-dioleoyl-*sn*-glycerol (DOG) were obtained from Avanti Polar Lipids, Inc. (Alabaster, AL) and other chemicals were obtained from Sigma-Aldrich (St. Louis, MO), unless specified. Stock solutions of POPC (13.15 mM), DOG (3.22 mM), and cholesterol (20 mM) were made in $CHCl_3$ (Burdick & Jackson, Mexico City, Mexico, high purity solvent) and stored in brown glass vials at –20 ^{0}C. Structures of FP analogs (synthetic amphipathic peptide with additional hydrophilic amino acids to their C-terminus) in the presence of phospholipid bilayer membranes or micelles, developed from NMR spectroscopy, are alpha-helical in their secondary structure with either a closed coiled-coil tertiary structure [62] or an open 'boomerang' shaped tertiary structure [19]. A 23 amino acid synthetic peptide corresponding to the X-31 FP domain (as studied in the Lorieau et al. [62]) was custom synthesized by GenScript, NJ and is labelled with tetra-methyl rhodamine (Sequence: GLFGAIAGFIENGWEGMIDGWYG [LYS(TRITC)]). Stock solutions of the peptide were prepared in DMSO and stored at – 20 ^{0}C. Since we wanted to compare the FP induced membrane poration with intact X-31 influenza virus induced poration[10], we chose to work with this sequence as it corresponds to the X-31 influenza viral fusion peptide. However, we also performed control poration experiments with a fusion peptide analog with sequence: GLFGAIAGFIEGGWTGMIDGWYG) [62] subsequently used in our molecular dynamic simulations. Our results showed the poration behavior of these two peptides is similar.

Preparation of Giant Unilamellar Vesicles (GUVs)

Giant unilamellar vesicles were prepared by the gel swelling method as described previously [63]. Briefly, to prepare GUVs of a specific lipid composition the required amount of lipid drawn from individual stock solutions was diluted into 200 µl of $CHCl_3$ to a concentration of 3.94 mM (3.35 mg/ml). The mixture was vortexed with ~10 µl of MeOH for ~2 min to avoid incomplete mixing and obtain a clear solution in $CHCl_3$. 10 µl of DiD (Invitrogen; prepared in DMSO as a 5 µM stock solution) was added to this lipid mixture and vortexed for ~2 min. The lipid mixture (in $CHCl_3$) was then deposited on a plasma cleaned (using a Harrick plasma cleaner, Ithaca, NY) microscope cover glass, coated with 5 % (w/w in ddH_2O) polyvinyl alcohol (Merck Millipore). The organic solvent was evaporated by a gentle stream of nitrogen and then stored in high vacuum

for 1 hour. The lipid film containing cover glass was then transferred to a 30-mm tissue culture dish. 500 µl of GUV formation buffer (1 mM EDTA, 1 mM HEDTA, 10 mM PIPES, 100 mM KCl, pH 7.4 with ~200 mM sucrose) was added covering the entire surface of the cover glass and allowed to incubate for 30 min in the dark. After 30 min, the GUVs were harvested by gently tapping the sides of the dish, then gently removing the GUV suspension using a 1 mL pipette without touching the surface and transferring to a 1.5 ml micro-centrifuge tube. The GUV suspension was stored at 4 ^{0}C until further use. The total lipid concentration of the GUV suspension was 1.35 mg/ml (1.58 mM). Typically, GUVs were made the same day of the experiment. To vary the spontaneous curvature systematically, POPC GUVs of varying concentrations of cholesterol, or DOG were prepared.

GUV poration assay

FP was added from the stock solution to a suspension of GUVs of defined compositions at a peptide to lipid ratio of 1:200 in a micro-centrifuge-tube. The total volume was diluted to 500 µl containing Alexa 488 or SRB. The mixture was then incubated at 37 ^{0}C for 15 min. While the peptide-GUV mixture was incubating, 500 µl of a 5 mg/ml β-casein solution was added to a delta-TPG 0.17 mm dish (Bioptechs, Butler, PA) allowed to sit for 10 min to passivate the glass surface, and then washed 10 times with ddH_2O. The GUV-peptide suspension was then vortexed for 30 s and transferred to this imaging dish. For a given lipid composition, ~100 GUVs were observed and scored based on whether they have undergone influx of Alexa 488. For kinetics measurements, the peptide was directly added to the chamber contacting GUVs while mounted on the microscope objective.

Confocal microscopy

GUVs were imaged on a Zeiss LSM 880 microscope using a 63× oil 1.4 NA Plan-Apochromat objective. The objective was connected to an objective heater (Bioptechs, Butler, PA) to maintain 37 ^{0}C inside the chamber (chamber temperature was verified with a microprobe). Alexa 488, SRB and DiD were excited with 488, 543 and 633 nm lasers respectively and detected using PMT detectors on separate imaging tracks.

Image, data, and statistical analyses

Microscopy images were analyzed using ImageJ (NIH). Data were analyzed using SigmaPlot (Systat Software, Inc., Chicago, IL), Excel (Microsoft, Inc., Redmond, WA), and MATLAB (The MathWorks, Inc., Natick, MA).

Molecular Dynamics Simulations

System preparation. Two membrane compositions were compared: pure POPC and 1:1 chol:POPC. Large membrane systems were constructed with 21, 10, 6, or 1 copies of the 23-residue FP (sequence: GLFGAIAGFIEGGWTGMIDGWYG) [62] placed in the top leaflet (21/0, 10/0, 6/0, and 1/0 FP distributions, respectively) of ~150x150 Å membranes. Smaller systems were also constructed with a single copy of the FP in each leaflet of ~75x75 Å bilayers (1/1 FP distribution). All systems were constructed using the CHARMM-GUI *Membrane Builder* [64-67] with a water thickness of 17.5 Å and 150 mM potassium chloride in the solvent. Simulations utilized the CHARMM36 force field [68,69] and TIP3P water model [70,71], and were all performed in the isothermal-isobaric (NPT) ensemble with a 2.0 fs time step.

Long time scale simulations. All large simulations were simulated first in OpenMM version 7.4.1 [72] using the Rickflow package version 0.7.0. OpenMM equilibration times were 750 ns for 21/0, 1000 ns for 10/0, and 100 ns each for 6/0 and 1/0 systems. Following this, because of the large fraction of peptides in the top leaflet, the 21/0 and 10/0 were simulated for 15 ns in CHARMM [73] using $P2_1$ boundary conditions [74] to allow lipids to equilibrate between leaflets. The number of lipids per leaflet was averaged over the last 7.5 ns of these $P2_1$ simulations, and representative frames with lipid distributions that matched this average were selected as starting coordinates for simulation on Anton 2 [75]. All large systems were then simulated on Anton 2 for production runs. The Anton 2 simulations times were 1 μs for 21/0, 5 μs for 10/0, and 2 μs each for 6/0 and 1/0. The 1/1 FP systems were simulated for 500 ns in OpenMM. For both system sizes, peptide-free systems of comparable size (150x150 Å and 75x75 Å) were simulated for 500 ns in OpenMM as controls.

All OpenMM simulations were performed at 310 K with the Nose-Hoover chain [76-78] velocity Verlet integrator implemented in openmmtools [79] and the Monte-Carlo membrane barostat [80]. Bonds with hydrogen were constrained using the SETTLE and CCMA algorithm [81,82]. A 12.0 Å cutoff was used, with a force-switching function from 8−12 Å. Long-range electrostatics were treated using the particle mesh Ewald method [83]. Coordinates and velocities were saved every 50 ps. Simulations on Anton 2 utilized the Multigrator framework [84] with the Nose-Hoover thermostat and semi-isotropic MTK barostat. An 8 Å cutoff distance was used, and long-range electrostatics were evaluated with the u-series method [75]. Coordinates were saved every 200 ps.

Constant electric field simulations. Short equilibrations were performed using the CHARMM-GUI six-step process. Subsequently, 30-ns MD simulations were carried out in CHARMM [73], utilizing the domain decomposition scheme [85]. Electrostatics were described using the particle-mesh Ewald (PME) method [83] with a κ value of 0.34 and spline order of 6, and van der Waals interactions were described using the Lennard-Jones potential with a 10-12 force switching function. Bonds involving hydrogen were kept constant with SHAKE [86]. The pressure was set to 1 atm using a frictionless piston with a mass of 1000 amu, and a Hoover thermostat was used to maintain a constant temperature of 310 K with a coupling constant of 4000 kcal mol^{-1} ps^{-2}. After the 30-ns simulations, both concentrations were simulated with 1.2 and 1.4 V electric fields, leading to four simulations. 1.2 V simulations were run for 9 ns and 1.4 V simulations for 5 ns. The electric field always pointed down into the membrane, and a harmonic restraint with force constant of 50 kcal mol^{-1} $Å^{-2}$ was used to maintain the membrane center-of-mass at $Z = 0$ Å. The same parameters were used as in the 30-ns MD simulations, except that the domain decomposition scheme was not used.

Simulation analysis. Thickness maps and leaflet position maps were calculated using the MEMBPLUGIN [87] extension for VMD, and all system snapshots were rendering using VMD [88]. Lipid density plots were calculated using LOOS [89,90]. Peptide clustering was assessed using the cluster module of the *freud* Python library[91]. All peptide heavy atoms were considered in the analysis, and a cutoff of 3.5 Å, consistent with a typical hydrogen bond donor-acceptor cutoff distance, was used to define points as belonging to the same cluster. Water, lipid, and peptide density distribution profiles were calculated using the density function in *cpptraj* [92]; only atoms within a cylinder of 30 Å centered about the origin (Figure S14) in the xy-plane were considered for this calculation. A bin width of 0.5 Å was used. FP-containing systems were first imaged such that the FP aggregate was centered at the origin, in the plane of the membrane. The PMF, $F(z)$, was calculated from the normalized water density distribution, $p(z)$:

$$F(z) = -k_B T \, ln(p(z)) \tag{2}$$

Permeability and partition coefficients. The inhomogeneous solubility diffusion (ISD) model [21] provides a simple relation between the free energy profile and the resistance to permeability, R. The permeability P in the ISD model is written:

$$\frac{1}{P} = e^{-\beta F_{ref}} \int_{-h/2}^{+h/2} \frac{e^{\beta F(z)}}{D_{\perp}(z)} dz \tag{3}$$

where $D_{\perp}(z)$ is the position dependent diffusion coefficient, $\beta = 1/k_B T$, h is the thickness of the bilayer, and F_{ref} is the reference free energy in the water phase that is set to zero. The diffusion constant is not calculated here and will be assumed to be a constant $\langle D \rangle$. The resistance is then defined from Equation 4 as:

$$\bar{R} = \int_{-h/2}^{+h/2} \mathrm{e}^{\beta F(z)} \mathrm{d}z = \langle D \rangle / P \tag{4}$$

Note that the preceding definition of $\bar{R}$ differs slightly from the usual definition of R, where the diffusion constant remains in the integral. The partition coefficient K is defined as the ratio of the permeant concentrations in the membrane (c_m) and in water (c_w). It can be evaluated from the free energy profile $F(z)$ as follows [22]:

$$K(h) = \frac{c_m(h)}{c_w} = \frac{1}{h} \int_{-h/2}^{+h/2} e^{\beta F((z) - F_{ref})} dz \tag{5}$$

where h is the membrane thickness. The permeant concentration in water is independent of membrane dimensions; its concentration in the membrane depends on h. The phosphate plane is the typical choice for thickness, but it is generally useful to plot $K(h)$ to confirm that it is relatively flat in the neighborhood of this plane. For the application here, the relative values of $K(h)$ in hydrocarbon region are of primary interest.

Spontaneous curvature calculation. For planar membranes, the spontaneous curvature c_0 is related to the derivative of the free energy with respect to curvature, $\bar{F}'(0)$, by [93]:

$$k_c c_0 = -\bar{F}'(0) \tag{6}$$

where k_c is the bending modulus. In planar membranes, $\bar{F}'(0)$, can be determined from the lateral pressure profile [94,95]:

$$\bar{F}'(0) = -\int_{-\infty}^{\infty} z[p_T(z) - p_N(z)] \mathrm{d}z \tag{7}$$

where $p_T(z)$ and $p_N(z)$ are the tangential and normal pressures. Lateral pressure profiles, $p_T(z) - p_N(z)$, for the small (1:1 FP) systems were calculated as described in Park, et al. [96] using a developmental version of CHARMM. Coordinates and velocities from the OpenMM simulations, taken every 2 ns, were used to seed very short (50 ps) simulations in CHARMM. $P(z)$ was calculated every 5 ps during these short simulations, then used to calculate $F'_m(0)$ for each leaflet. Because the equation of $F'_m(0)$ and the first moment of the bilayer lateral pressure profile (Equation 7) assumes a planar membrane, these calculations were only performed in the small (1:1 FP) systems where no explicit curvature of the membrane was observed. For the pure POPC

systems, the bilayer bending constant reported by Venable et al. of $K_{c,b}$ = 19.1 kcal/mol[21] was used. Since we were interested in the spontaneous curvature of a leaflet, rather than the bilayer as a whole, these calculations used $K_{c,m} = K_{c,b}/2$ = 9.55 kcal/mol. The polymer brush method [97] used by Venable et al. is well validated for saturated lipids but is known to have limited application to mixtures containing cholesterol [98]. While no experimental K_c exist for mixtures of cholesterol and POPC, Chen and Rand noted a 122% increase in K_c for DOPC with the addition of 50 mol % cholesterol [2]. Estimating a similar increase in K_c for POPC yields $K_{c,m}$ = 11.67 kcal/mol for 1:1 chol:POPC, which is what we used in this work. Finally, to estimate the difference in spontaneous curvature due to changes in $F'(0)$, we assume K_c is unchanged by addition of a single peptide; therefore, any systematic error of the estimated K_c for the chol:POPC mixture would effect both estimated spontaneous curvature values equally.

Analytical theory. Isolated peptide model of pore formation. The lipid monolayer is assumed to be a continuum elastic medium. To describe the structure of the pore edge, we have modified the classical Helfrich energy functional by applying it separately to each monolayer of the membrane. Specifically, the membrane is divided into two regions: the highly deformed pore edge and the undeformed flat membrane, which allows us to focus only on the edge region. We model the edge shape as a half-torus characterized by two radii – one equal to the pore radius R in its equatorial plane, and the other equal to the monolayer thickness h. This allows joining smoothly the toroid and planar membrane regions. The elastic energy of the membrane with respect to the flat state can be written as:

$$E_{el} = \int \frac{B}{2}\left(J - J_s\right)^2 dS - \int \frac{B}{2} J_s^2 dS, \tag{8}$$

where J is the local curvature of the membrane monolayer, B is its bending rigidity, J_s is monolayer spontaneous curvature, which depends on the monolayer local composition; integration is performed over the area of the membrane monolayer surface. The spontaneous curvature of the monolayer depends on the local composition. We use the common linear model to describe the dependence of the spontaneous curvature on the component concentrations:

$$J_s = \sum_i \phi_i J_{0i}, \tag{9}$$

where ϕ_i are the local surface coverage of the components, and J_{0i} are the spontaneous curvatures of the components. The latter parameters for the lipid components have been measured

experimentally[2,13,99]. Peptides do not form monolayers so their spontaneous curvatures cannot be assigned in the same manner as for the lipids. However, in terms of average action, this parameter can be attributed to a peptide's ability to generate curvature in the lipid membranes. The spontaneous curvature of the peptide can be roughly estimated from the dimensionality considerations as $J_{0FP} = \frac{p_p}{a_p} n_b$, where P_p is the peptide boundary length (~4 nm), a_p is the peptide area (~4 nm^2), and n_b is the lipid tail inclination induced by the boundary of the peptide.

Alteration of the local composition of the lipid monolayer can adjust the spontaneous curvature to fit the local curvature of its surface, thus relaxing the elastic energy. However, this lipid desegregation leads to a decrease of the mixing entropy and corresponding increase of free energy density, which can be expressed in the following form[100]

$$F_{mix} = \frac{1}{a_p}\left(\phi \ln\left(\frac{\phi}{\phi_0}\right) + (1-\phi)\ln\left(\frac{1-\phi}{1-\phi_0}\right)\right) + (1-\phi)\frac{1}{a_l}\left(c\ln\left(\frac{c}{c_0}\right) + (1-c)\ln\left(\frac{1-c}{1-c_0}\right)\right), \quad (10)$$

where a_p is the area per peptide; a_l is the average area per lipid molecule; ϕ is the local area fraction of the FP on the membrane; c is the local concentration of the lipid components in the binary lipid mixture; ϕ_0 and c_0 are average peptide area fraction and lipid concentration, respectively. Altering the local concentration of lipid components also induces elastic stress in the lipid membrane, leading to the following energy penalty:

$$E_{el,mix} = \int \frac{B}{2}\left(J_{s0} - J_s\right)^2 dS, \quad (11)$$

where J_{s0} is the average spontaneous curvature of the lipid monolayer. Thus, the total energy of the monolayer patch consists of three contributions: elastic deformations (Eq. 8), mixing entropy penalty (Eq. 10), and mixing elasticity penalty (Eq. 11):

$$E_{tot} = E_{el} + F_{mix} + E_{el,mix}. \quad (12)$$

Minimizing the total energy E_{tot} with respect to the component distribution at a given pore radius gives the pore energy. The pore opening trajectory starts with the formation of the bilayer-spanning hydrophobic pore[23,30]; its energy has an additional contribution arising from unfavorable contact of lipid tails with water. This contribution can be expressed as:

$$E_H = \sigma_h 2\pi R \cdot 2h \frac{I_1(R)}{I_0(R)}, \quad (13)$$

where σ_h is the surface tension at the macroscopic interface of lipid tails and water; $\xi_h \sim 1$ nm is the characteristic length of hydrophobic interactions[101]; $I_{1,0}$ are modified Bessel functions of the first and zeroth order, respectively. To form the bilayer-spanning conductive hydrophilic pore, the boundary lipids of the initial hydrophobic defect should reorient and deform to assemble the inverted (hydrophilic) pore edge. This transition occurs at the radius where the energies of the hydrophobic defect and hydrophilic pore match. For the chosen parameters, the transition from hydrophobic defect to hydrophilic pore occurs at $R \sim 0.65$ nm. The average area fraction of the peptide found from the MD simulations is equal to $c_p = 0.037$ for 0% cholesterol and $c_p = 0.045$ for 50% cholesterol. We have interpolated that dependence linearly obtaining the following dependence: $\phi_0 = 0.037\times(1 + 0.44c_p)$. The monolayer hydrophobic thickness is set to 1.5 nm. Although the spontaneous curvature changes significantly both the energy and equilibrium radius of the metastable pore, it weakly affects the position of the first energy barrier[23]. At a larger radius ($R \sim 1$ nm), the hydrophilic pore has a metastable state, which characterized by a local minimum of the total energy (Figure 8). This state has a finite lifetime and can lead to vesicle leakage. The total number of such metastable defects is governed by their energy, E_{pore}, and is proportional to the Boltzmann factor e^{-E_{pore}/k_BT}. That leads to the reasonable assumption that the fraction of leaky vesicles p is proportional to the Boltzmann factor, $p \sim e^{-E_{pore}/k_BT}$. Therefore, by calculating the pore energy profile at different lipid compositions, we can predict the dependence of the fraction of leaky vesicles on the lipid composition, assuming the proportionality coefficient to be independent of the composition.

Analytical theory. Calculation of the dependence of pore energy on the cluster size. We modeled FP cluster as a monolayer region that is thinner and stiffer than the lipid monolayer in the framework of continuum theory[102]. Due to smaller thickness of the FP monolayer, a hydrophobic mismatch appears at the cluster boundary, where the lipid bilayer of thickness $2h$ contacts with "hybrid" bilayer consisting of lipid monolayer and monolayer of fusion peptides, of the total thickness $h + h_p$. The thickness mismatch is compensated at the expense of elastic deformations arising at the cluster boundary. The characteristic length of deformations is of the order of units of nanometers [103]. Formation of the hydrophobic defect in the center of the cluster is also accompanied by elastic deformations of the adjacent "hybrid" bilayer; the deformations also spread to about several nanometers around the hydrophobic defect. When the cluster radius is

small enough, the deformations induced by the hydrophobic defect and by the cluster boundary overlap, leading to effective membrane-mediated interaction of the defect and boundary. We calculated the dependence of the energy of the cluster with hydrophobic defect of fixed radius (r_h = 0.65 nm) in its center, on the radius of the cluster, R_c. The calculations were performed essentially as described in [104,105] . The hydrophobic defect was modeled as a water-filled cylinder with hydrophobic walls; the system had an opportunity to optimize the height of the hydrophobic defect. Defect's energy was calculated based on the Marčelja theory [23,25,30]. To obtain quantitative results, we used the following values of the parameters: bending modulus of lipid monolayer $B = 10\ k_BT$ ($k_BT \sim 4.14 \cdot 10^{-21}$ J at room temperature, $T = 300$ K); hydrophobic thickness of lipid monolayer h = 1.5 nm; bending modulus of FP monolayer $B_{\mathrm{FP}} = 10$, 20, or 40 k_BT; hydrophobic thickness of FP monolayer $h_p = 1.1$ nm.

Analytical theory. PFM analysis. Water wire energies W_{wire} were normalized by the energy of the water cylinder E_H in the hydrophobic media, calculated based on the Marčelja theory [23,25,30] in accordance with Eq. (13).

We consider the POPC membrane as a reference system. Its hydrophobic thickness is taken equal to ~ 3 nm, the macroscopic surface tension of water-lipid tails interface is taken to be equal to $\sigma_h = 10\ k_BT/\mathrm{nm}^2 = 40$ mN/m. The energy of the corresponding hydrophobic defect with a 13 Å diameter and 3 nm length equals to $E_{POPC} = 38\ k_BT = 22$ kcal/mol. We integrate the water PFM energy profiles for all membrane compositions and obtain four water wire energies W_{POPC}, $W_{POPC+Ch}$, $W_{POPC+FP}$, $W_{POPC+Ch+FP}$, respectively, in accordance with eq. (1). Further, we introduce the proportionality coefficient between W_{POPC} and E_{POPC}: $\alpha = W_{POPC}/E_{POPC}$. Parameter α accounts for the difference in the number of hydrogen bonds and water molecules in the water wire and hydrophobic defect of 13 Å diameter. We assume that α does not depend on the nature of the bilayer, therefore being universal proportionality coefficient between $E_{wire,i}$ and W_i for membranes of all considered compositions: $\alpha = W_{POPC}/E_{POPC} = W_{POPC+Ch}/E_{POPC+Ch} = W_{POPC+FP}/E_{POPC+FP}$.

Author Contributions:
SH, PSB, and JZ designed and carried out the microscopy experiments. AR, RWP, and EW designed and carried out the MD simulations. SAA and TRG developed the analytical theory. All authors contributed to writing the paper.

Acknowledgments:

This work was supported by the Intramural Programs of the *Eunice Kennedy Shriver* National Institute of Child Health and Human Development and the National Heart Lung and Blood Institute of the National Institutes of Health, Bethesda MD, USA, and used high performance computational resources at the National Institutes of Health (NHLBI LoBoS and HPC Biowulf cluster). Anton 2 computer time was provided by the Pittsburgh Supercomputing Center (PSC) through Grant *R01GM116961* from the National Institutes of Health. The Anton 2 machine at PSC was generously made available by D.E. Shaw Research. TRG is grateful to the Russian Science Foundation (Project No. 19-74-00152) for support. We thank Dr. Matthias Garten for helpful discussion regarding GUV preparation and Dr. Adriaan Bax for a kind gift of the fusion peptide analog used in a control experiment.

References

1 Venable, R. M., Brown, F. L. H. & Pastor, R. W. Mechanical properties of lipid bilayers from molecular dynamics simulation. *Chemistry and Physics of Lipids* **192**, 60-74, doi:https://doi.org/10.1016/j.chemphyslip.2015.07.014 (2015).

2 Chen, Z. & Rand, R. P. The influence of cholesterol on phospholipid membrane curvature and bending elasticity. *Biophysical journal* **73**, 267-276, doi:10.1016/s0006-3495(97)78067-6 (1997).

3 Brunner, J., Zugliani, C. & Mischler, R. Fusion activity of influenza virus PR8/34 correlates with a temperature-induced conformational change within the hemagglutinin ectodomain detected by photochemical labeling. *Biochemistry* **30**, 2432-2438 (1991).

4 Durrer, P. *et al.* H+-induced membrane insertion of influenza virus hemagglutinin involves the HA2 amino-terminal fusion peptide but not the coiled coil region. *The Journal of biological chemistry* **271**, 13417-13421, doi:10.1074/jbc.271.23.13417 (1996).

5 Gething, M. J., Doms, R. W., York, D. & White, J. Studies on the mechanism of membrane fusion: site-specific mutagenesis of the hemagglutinin of influenza virus. *The Journal of cell biology* **102**, 11-23, doi:10.1083/jcb.102.1.11 (1986).

6 Harrison, S. C. Viral membrane fusion. *Virology* **479-480**, 498-507, doi:10.1016/j.virol.2015.03.043 (2015).

7 Cross, K. J., Langley, W. A., Russell, R. J., Skehel, J. J. & Steinhauer, D. A. Composition and functions of the influenza fusion peptide. *Protein and peptide letters* **16**, 766-778 (2009).

8 Lear, J. D. & DeGrado, W. F. Membrane binding and conformational properties of peptides representing the NH2 terminus of influenza HA-2. *The Journal of biological chemistry* **262**, 6500-6505 (1987).

9 Chlanda, P. *et al.* The hemifusion structure induced by influenza virus haemagglutinin is determined by physical properties of the target membranes. *Nature microbiology* **1**, 16050, doi:10.1038/nmicrobiol.2016.50 (2016).

10 Frolov, V. A., Dunina-Barkovskaya, A. Y., Samsonov, A. V. & Zimmerberg, J. Membrane permeability changes at early stages of influenza hemagglutinin-mediated fusion. *Biophysical journal* **85**, 1725-1733, doi:10.1016/s0006-3495(03)74602-5 (2003).

11 Shangguan, T., Alford, D. & Bentz, J. Influenza-virus-liposome lipid mixing is leaky and largely insensitive to the material properties of the target membrane. *Biochemistry* **35**, 4956-4965, doi:10.1021/bi9526903 (1996).

12 Haldar, S., Mekhedov, E., McCormick, C. D., Blank, P. S. & Zimmerberg, J. Lipid-dependence of target membrane stability during influenza viral fusion. *Journal of cell science* **132**, doi:10.1242/jcs.218321 (2018).

13 Kollmitzer, B., Heftberger, P., Rappolt, M. & Pabst, G. Monolayer spontaneous curvature of raft-forming membrane lipids. *Soft Matter* **9**, 10877-10884, doi:10.1039/c3sm51829a (2013).

14 Szule, J. A., Fuller, N. L. & Rand, R. P. The effects of acyl chain length and saturation of diacylglycerols and phosphatidylcholines on membrane monolayer curvature. *Biophysical journal* **83**, 977-984, doi:10.1016/s0006-3495(02)75223-5 (2002).

15 Kumaraswamy, P. A generalized probability density function for double-bounded random processes. *Journal of Hydrology* **46**, 79-88, doi:https://doi.org/10.1016/0022-1694(80)90036-0 (1980).

16 Jones, M. C. Kumaraswamy's distribution: A beta-type distribution with some tractability advantages. *Statistical Methodology* **6**, 70-81, doi:https://doi.org/10.1016/j.stamet.2008.04.001 (2009).

17 Wheaten, S. A., Lakshmanan, A. & Almeida, P. F. Statistical analysis of peptide-induced graded and all-or-none fluxes in giant vesicles. *Biophysical journal* **105**, 432-443, doi:10.1016/j.bpj.2013.05.055 (2013).
18 Apellaniz, B., Nieva, J. L., Schwille, P. & Garcia-Saez, A. J. All-or-none versus graded: single-vesicle analysis reveals lipid composition effects on membrane permeabilization. *Biophysical journal* **99**, 3619-3628, doi:10.1016/j.bpj.2010.09.027 (2010).
19 Han, X., Bushweller, J. H., Cafiso, D. S. & Tamm, L. K. Membrane structure and fusion-triggering conformational change of the fusion domain from influenza hemagglutinin. *Nature structural biology* **8**, 715-720, doi:10.1038/90434 (2001).
20 Diamond, J. M. & Katz, Y. Interpretation of nonelectrolyte partition coefficients between dimyristoyl lecithin and water. *J Membr Biol* **17**, 121-154, doi:10.1007/bf01870176 (1974).
21 Venable, R. M., Krämer, A. & Pastor, R. W. Molecular Dynamics Simulations of Membrane Permeability. *Chem Rev* **119**, 5954-5997, doi:10.1021/acs.chemrev.8b00486 (2019).
22 Ghysels, A. *et al.* Permeability of membranes in the liquid ordered and liquid disordered phases. *Nat Commun* **10**, 5616, doi:10.1038/s41467-019-13432-7 (2019).
23 Akimov, S. A. *et al.* Pore formation in lipid membrane I: Continuous reversible trajectory from intact bilayer through hydrophobic defect to transversal pore. *Sci Rep* **7**, 12152, doi:10.1038/s41598-017-12127-7 (2017).
24 Helfrich, W. Elastic properties of lipid bilayers: theory and possible experiments. *Z Naturforsch C* **28**, 693-703, doi:10.1515/znc-1973-11-1209 (1973).
25 Marčelja, S. Structural contribution to solute-solute interaction. *Croatica Chemica Acta* **49**, 347-358 (1977).
26 Kuzmin, P. I., Zimmerberg, J., Chizmadzhev, Y. A. & Cohen, F. S. A quantitative model for membrane fusion based on low-energy intermediates. *Proceedings of the National Academy of Sciences of the United States of America* **98**, 7235-7240, doi:10.1073/pnas.121191898 (2001).
27 Molotkovsky, R. J. *et al.* Switching between Successful and Dead-End Intermediates in Membrane Fusion. *Int J Mol Sci* **18**, doi:10.3390/ijms18122598 (2017).
28 Shnyrova, A. V. *et al.* Geometric catalysis of membrane fission driven by flexible dynamin rings. *Science* **339**, 1433-1436, doi:10.1126/science.1233920 (2013).
29 Akimov, S. A., Aleksandrova, V. V., Galimzyanov, T. R., Bashkirov, P. V. & Batishchev, O. V. Mechanism of pore formation in stearoyl-oleoyl-phosphatidylcholine membranes subjected to lateral tension. *Biochemistry (Moscow), Supplement Series A: Membrane and Cell Biology* **11**, 193-205, doi:10.1134/s1990747817030023 (2017).
30 Akimov, S. A. *et al.* Pore formation in lipid membrane II: Energy landscape under external stress. *Sci Rep* **7**, 12509, doi:10.1038/s41598-017-12749-x (2017).
31 Skehel, J. J. *et al.* Changes in the conformation of influenza virus hemagglutinin at the pH optimum of virus-mediated membrane fusion. *Proceedings of the National Academy of Sciences* **79**, 968-972, doi:10.1073/pnas.79.4.968 (1982).
32 Sato, S. B., Kawasaki, K. & Ohnishi, S. Hemolytic activity of influenza virus hemagglutinin glycoproteins activated in mildly acidic environments. *Proceedings of the National Academy of Sciences* **80**, 3153-3157, doi:10.1073/pnas.80.11.3153 (1983).
33 Ruigrok, R. W. *et al.* Studies on the structure of the influenza virus haemagglutinin at the pH of membrane fusion. *J Gen Virol* **69 (Pt 11)**, 2785-2795, doi:10.1099/0022-1317-69-11-2785 (1988).
34 Arai, Y. T., Kondo, A. & Suzuki, K. Demonstration of non-infectious hemagglutinating particles of rabies virus and isolation of the hemagglutinin by disruption of the virion with Nonidet P-40. *Arch Virol* **51**, 335-345, doi:10.1007/bf01317937 (1976).

35 Behling, U. H., Campbell, B., Chang, C.-M., Rumpf, C. & Nowotny, A. Synthetic Glycolipid Adjuvants. *The Journal of Immunology* **117**, 847-851 (1976).
36 Ting Hui, L. *et al.* Improving immunogenicity of influenza virus H7N9 recombinant hemagglutinin for vaccine development. *Vaccine* **37**, 1897-1903, doi:https://doi.org/10.1016/j.vaccine.2018.09.034 (2019).
37 Trudel, M., Nadon, F., Comtois, R., Ravaoarinoro, M. & Payment, P. Antibody response to rubella virus proteins in different physical forms. *Antiviral Res* **2**, 347-354, doi:10.1016/0166-3542(82)90004-3 (1982).
38 Trudel, M., Marchessault, F. & Payment, P. Characterisation of rubella virus hemagglutinin rosettes. *J Virol Methods* **2**, 195-201, doi:10.1016/0166-0934(81)90009-4 (1981).
39 Banani, S. F., Lee, H. O., Hyman, A. A. & Rosen, M. K. Biomolecular condensates: organizers of cellular biochemistry. *Nat Rev Mol Cell Biol* **18**, 285-298, doi:10.1038/nrm.2017.7 (2017).
40 Murata, M., Takahashi, S., Kagiwada, S., Suzuki, A. & Ohnishi, S. pH-dependent membrane fusion and vesiculation of phospholipid large unilamellar vesicles induced by amphiphilic anionic and cationic peptides. *Biochemistry* **31**, 1986-1992 (1992).
41 Lagüe, P., Roux, B. & Pastor, R. W. Molecular Dynamics Simulations of the Influenza Hemagglutinin Fusion Peptide in Micelles and Bilayers: Conformational Analysis of Peptide and Lipids. *Journal of Molecular Biology* **354**, 1129-1141, doi:https://doi.org/10.1016/j.jmb.2005.10.038 (2005).
42 Sodt, Alexander J. & Pastor, Richard W. Molecular Modeling of Lipid Membrane Curvature Induction by a Peptide: More than Simply Shape. *Biophysical journal* **106**, 1958-1969, doi:https://doi.org/10.1016/j.bpj.2014.02.037 (2014).
43 Siegel, D. P. & Epand, R. M. Effect of influenza hemagglutinin fusion peptide on lamellar/inverted phase transitions in dipalmitoleoylphosphatidylethanolamine: implications for membrane fusion mechanisms. *Biochimica et biophysica acta* **1468**, 87-98 (2000).
44 Tenchov, B. G., MacDonald, R. C. & Lentz, B. R. Fusion peptides promote formation of bilayer cubic phases in lipid dispersions. An x-ray diffraction study. *Biophysical journal* **104**, 1029-1037, doi:10.1016/j.bpj.2012.12.034 (2013).
45 Wasilewski, S., Calder, L. J., Grant, T. & Rosenthal, P. B. Distribution of surface glycoproteins on influenza A virus determined by electron cryotomography. *Vaccine* **30**, 7368-7373, doi:10.1016/j.vaccine.2012.09.082 (2012).
46 Hamm, M. & Kozlov, M. M. Elastic energy of tilt and bending of fluid membranes. *Eur. Phys. J. E* **3**, 323-335 (2000).
47 Ting, C. L., Awasthi, N., Müller, M. & Hub, J. S. Metastable Prepores in Tension-Free Lipid Bilayers. *Phys Rev Lett* **120**, 128103, doi:10.1103/PhysRevLett.120.128103 (2018).
48 Sengel, J. T. & Wallace, M. I. Measuring the potential energy barrier to lipid bilayer electroporation. *Philos Trans R Soc Lond B Biol Sci* **372**, doi:10.1098/rstb.2016.0227 (2017).
49 Dixit, M. & Lazaridis, T. Free energy of hydrophilic and hydrophobic pores in lipid bilayers by free energy perturbation of a restraint. *J Chem Phys* **153**, 054101, doi:10.1063/5.0016682 (2020).
50 Bennett, W. F., Sapay, N. & Tieleman, D. P. Atomistic simulations of pore formation and closure in lipid bilayers. *Biophysical journal* **106**, 210-219, doi:10.1016/j.bpj.2013.11.4486 (2014).
51 Illya, G. & Deserno, M. Coarse-grained simulation studies of peptide-induced pore formation. *Biophysical journal* **95**, 4163-4173, doi:10.1529/biophysj.108.131300 (2008).
52 Müller, M., Katsov, K. & Schick, M. New mechanism of membrane fusion. *The Journal of Chemical Physics* **116**, 2342-2345, doi:10.1063/1.1448496 (2002).
53 Müller, M., Katsov, K. & Schick, M. A New Mechanism of Model Membrane Fusion Determined from Monte Carlo Simulation. *Biophysical journal* **85**, 1611-1623, doi:https://doi.org/10.1016/S0006-3495(03)74592-5 (2003).

54 Katsov, K., Müller, M. & Schick, M. Field Theoretic Study of Bilayer Membrane Fusion: II. Mechanism of a Stalk-Hole Complex. *Biophysical journal* **90**, 915-926, doi:https://doi.org/10.1529/biophysj.105.071092 (2006).
55 Schick, M. Membrane Fusion: the Emergence of a New Paradigm. *Journal of Statistical Physics* **142**, 1317-1323, doi:10.1007/s10955-010-0111-9 (2011).
56 Qiao, H., Armstrong, R. T., Melikyan, G. B., Cohen, F. S. & White, J. M. A specific point mutant at position 1 of the influenza hemagglutinin fusion peptide displays a hemifusion phenotype. *Mol Biol Cell* **10**, 2759-2769, doi:10.1091/mbc.10.8.2759 (1999).
57 Sun, X. & Whittaker, G. R. Role for influenza virus envelope cholesterol in virus entry and infection. *J Virol* **77**, 12543-12551, doi:10.1128/jvi.77.23.12543-12551.2003 (2003).
58 Razinkov, V. I., Melikyan, G. B., Epand, R. M., Epand, R. F. & Cohen, F. S. Effects of spontaneous bilayer curvature on influenza virus-mediated fusion pores. *J Gen Physiol* **112**, 409-422, doi:10.1085/jgp.112.4.409 (1998).
59 Bashkirov, P. V. *et al.* GTPase cycle of dynamin is coupled to membrane squeeze and release, leading to spontaneous fission. *Cell* **135**, 1276-1286, doi:10.1016/j.cell.2008.11.028 (2008).
60 Leikina, E. *et al.* Myomaker and Myomerger Work Independently to Control Distinct Steps of Membrane Remodeling during Myoblast Fusion. *Dev Cell* **46**, 767-780.e767, doi:10.1016/j.devcel.2018.08.006 (2018).
61 Petrany, M. J. & Millay, D. P. Cell Fusion: Merging Membranes and Making Muscle. *Trends in Cell Biology* **29**, 964-973, doi:https://doi.org/10.1016/j.tcb.2019.09.002 (2019).
62 Lorieau, J. L., Louis, J. M. & Bax, A. The complete influenza hemagglutinin fusion domain adopts a tight helical hairpin arrangement at the lipid:water interface. *Proceedings of the National Academy of Sciences of the United States of America* **107**, 11341-11346, doi:10.1073/pnas.1006142107 (2010).
63 Weinberger, A. *et al.* Gel-assisted formation of giant unilamellar vesicles. *Biophysical journal* **105**, 154-164, doi:10.1016/j.bpj.2013.05.024 (2013).
64 Jo, S., Kim, T., Iyer, V. G. & Im, W. CHARMM-GUI: a Web-based Graphical User Interface for CHARMM. *J Comput Chem* **29**, 1859-1865, doi:10.1002/jcc.20945 (2008).
65 Jo, S., Lim, J. B., Klauda, J. B. & Im, W. CHARMM-GUI Membrane Builder for Mixed Bilayers and Its Application to Yeast Membranes. *Biophysical Journal* **97**, 50-58, doi:10.1016/j.bpj.2009.04.013 (2009).
66 Jo, S., Kim, T. & Im, W. Automated Builder and Database of Protein/Membrane Complexes for Molecular Dynamics Simulations. *Plos One* **2**, 9, doi:10.1371/journal.pone.0000880 (2007).
67 Wu, E. L. *et al.* CHARMM-GUI Membrane Builder Toward Realistic Biological Membrane Simulations. *Journal of Computational Chemistry* **35**, 1997-2004, doi:10.1002/jcc.23702 (2014).
68 Klauda, J. B. *et al.* Update of the CHARMM All-atom Additive Force Field for Lipids: Validation on Six Lipid Types. *Journal of Physical Chemistry B* **114**, 7830-7843 (2010).
69 Lim, J. B., Rogaski, B. & Klauda, J. B. Update of the Cholesterol Force Field Parameters in CHARMM. *J. Phys. Chem. B* **116**, 203-210, doi:10.1021/jp207925m (2012).
70 Jorgensen, W. L., Chandrasekhar, J., Madura, J. D., Impey, R. W. & Klein, M. L. Comparison of Simple Potential Functions for Simulating Liquid Water. *Journal of Chemical Physics* **79**, 926-935 (1983).
71 Durell, S. R., Brooks, B. R. & Bennaim, A. Solvent-Induced Forces between Two Hydrophilic Groups. *Journal of Physical Chemistry* **98**, 2198-2202 (1994).
72 Eastman, P. *et al.* OpenMM 7: Rapid development of high performance algorithms for molecular dynamics. *PLoS Comput Biol* **13**, e1005659, doi:10.1371/journal.pcbi.1005659 (2017).
73 Brooks, B. R. *et al.* CHARMM: The Biomolecular Simulation Program. *Journal of Computational Chemistry* **30**, 1545-1614 (2009).

74 Dolan, E. A., Venable, R. M., Pastor, R. W. & Brooks, B. R. Simulations of membranes and other interfacial systems using P2(1) and Pc periodic boundary conditions. *Biophysical journal* **82**, 2317-2325, doi:10.1016/s0006-3495(02)75577-x (2002).
75 Shaw, D. E. *et al.* in *SC '14: Proceedings of the International Conference for High Performance Computing, Networking, Storage and Analysis.* 41-53.
76 Hoover, W. G. Canonical dynamics: Equilibrium phase-space distributions. *Physical Review A* **31**, 1695-1697, doi:10.1103/PhysRevA.31.1695 (1985).
77 Martyna, G. J., Klein, M. L. & Tuckerman, M. Nosé–Hoover chains: The canonical ensemble via continuous dynamics. *The Journal of Chemical Physics* **97**, 2635-2643, doi:10.1063/1.463940 (1992).
78 Nosé, S. A molecular dynamics method for simulations in the canonical ensemble. *Molecular Physics* **52**, 255-268, doi:10.1080/00268978400101201 (1984).
79 choderalab/openmmtools: 0.19.0 - Multiple alchemical regions v. 0.19.0 (Zenodo, 2019).
80 Chow, K.-H. & Ferguson, D. M. Isothermal-isobaric molecular dynamics simulations with Monte Carlo volume sampling. *Computer Physics Communications* **91**, 283-289, doi:https://doi.org/10.1016/0010-4655(95)00059-O (1995).
81 Eastman, P. & Pande, V. S. Constant Constraint Matrix Approximation: A Robust, Parallelizable Constraint Method for Molecular Simulations. *Journal of Chemical Theory and Computation* **6**, 434-437, doi:10.1021/ct900463w (2010).
82 Miyamoto, S. & Kollman, P. A. Settle: An analytical version of the SHAKE and RATTLE algorithm for rigid water models. *Journal of Computational Chemistry* **13**, 952-962, doi:10.1002/jcc.540130805 (1992).
83 Darden, T., York, D. & Pedersen, L. Particle Mesh Ewald - an NLog(N) Method for Ewald Sums in Large Systems. *Journal of Chemical Physics* **98**, 10089-10092 (1993).
84 Lippert, R. A. *et al.* Accurate and efficient integration for molecular dynamics simulations at constant temperature and pressure. *J Chem Phys* **139**, 164106, doi:10.1063/1.4825247 (2013).
85 Hynninen, A. P. & Crowley, M. F. New faster CHARMM molecular dynamics engine. *J Comput Chem* **35**, 406-413, doi:10.1002/jcc.23501 (2014).
86 Kräutler, V., van Gunsteren Wilfred, F. & Hünenberger Philippe, H. A fast SHAKE algorithm to solve distance constraint equations for small molecules in molecular dynamics simulations. *Journal of Computational Chemistry* **22**, 501-508, doi:10.1002/1096-987X(20010415)22:5<501::AID-JCC1021>3.0.CO;2-V (2001).
87 Guixà-González, R. *et al.* MEMBPLUGIN: studying membrane complexity in VMD. *Bioinformatics* **30**, 1478-1480, doi:10.1093/bioinformatics/btu037 (2014).
88 Humphrey, W., Dalke, A. & Schulten, K. VMD: Visual molecular dynamics. *Journal of Molecular Graphics* **14**, 33-38, doi:https://doi.org/10.1016/0263-7855(96)00018-5 (1996).
89 Romo, T. D., Grossfield, A. & Ieee. in *2009 Annual International Conference of the Ieee Engineering in Medicine and Biology Society, Vols 1-20 IEEE Engineering in Medicine and Biology Society Conference Proceedings* 2332-2335 (2009).
90 Romo, T. D., Leioatts, N. & Grossfield, A. Lightweight Object Oriented Structure Analysis: Tools for Building Tools to Analyze Molecular Dynamics Simulations. *Journal of Computational Chemistry* **35**, 2305-2318, doi:10.1002/jcc.23753 (2014).
91 Ramasubramani, V. *et al.* freud: A software suite for high throughput analysis of particle simulation data. *Computer Physics Communications* **254**, doi:10.1016/j.cpc.2020.107275 (2020).
92 Roe, D. R. & Cheatham, T. E., 3rd. PTRAJ and CPPTRAJ: Software for Processing and Analysis of Molecular Dynamics Trajectory Data. *J Chem Theory Comput* **9**, 3084-3095, doi:10.1021/ct400341p (2013).

93 Sodt, A. J. & Pastor, R. W. Molecular modeling of lipid membrane curvature induction by a peptide: more than simply shape. *Biophysical journal* **106**, 1958-1969, doi:10.1016/j.bpj.2014.02.037 (2014).
94 Goetz, R. & Lipowsky, R. Computer simulations of bilayer membranes: Self-assembly and interfacial tension. *The Journal of Chemical Physics* **108**, 7397-7409, doi:10.1063/1.476160 (1998).
95 Szleifer, I., Kramer, D., Ben-Shaul, A., Gelbart, W. M. & Safran, S. A. Molecular theory of curvature elasticity in surfactant films. *The Journal of Chemical Physics* **92**, 6800-6817, doi:10.1063/1.458267 (1990).
96 Park, S., Im, W., Pastor, R.W. Developing Initial Conditions for Simulations of Asymmetric Membranes: A Practical Recommendation. *Biophys. J. in revision* (2021).
97 Rawicz, W., Olbrich, K. C., McIntosh, T., Needham, D. & Evans, E. Effect of chain length and unsaturation on elasticity of lipid bilayers. *Biophys. J.* **79**, 328-339 (2000).
98 Pan, J., Tristram-Nagle, S. & Nagle, J. F. Effect of cholesterol on structural and mechanical properties of membranes depends on lipid chain saturation. *Phys Rev E Stat Nonlin Soft Matter Phys* **80**, 021931, doi:10.1103/PhysRevE.80.021931 (2009).
99 Chen, Z. & Rand, R. P. The influence of cholesterol on phospholipid membrane curvature and bending elasticity. *Biophys. J.* **73**, 267-276 (1997).
100 Boucrot, E. *et al.* Membrane fission is promoted by insertion of amphipathic helices and is restricted by crescent BAR domains. *Cell* **149**, 124-136, doi:10.1016/j.cell.2012.01.047 (2012).
101 Israelachvili, J. & Pashley, R. The hydrophobic interaction is long range, decaying exponentially with distance. *Nature* **300**, 341-342, doi:10.1038/300341a0 (1982).
102 Hamm, M. & Kozlov, M. M. Elastic energy of tilt and bending of fluid membranes. *The European Physical Journal E* **3**, 323-335, doi:10.1007/s101890070003 (2000).
103 Kondrashov, O. V., Galimzyanov, T. R., Jiménez-Munguía, I., Batishchev, O. V. & Akimov, S. A. Membrane-mediated interaction of amphipathic peptides can be described by a one-dimensional approach. *Physical Review E* **99**, 022401, doi:10.1103/PhysRevE.99.022401 (2019).
104 Galimzyanov, T. R. *et al.* Elastic Membrane Deformations Govern Interleaflet Coupling of Lipid-Ordered Domains. *Physical Review Letters* **115**, 088101, doi:10.1103/PhysRevLett.115.088101 (2015).
105 Galimzyanov, T. R., Molotkovsky, R. J., Cohen, F. S., Pohl, P. & Akimov, S. A. Galimzyanov et al. Reply. *Phys Rev Lett* **116**, 079802, doi:10.1103/PhysRevLett.116.079802 (2016).

Supplementary Materials

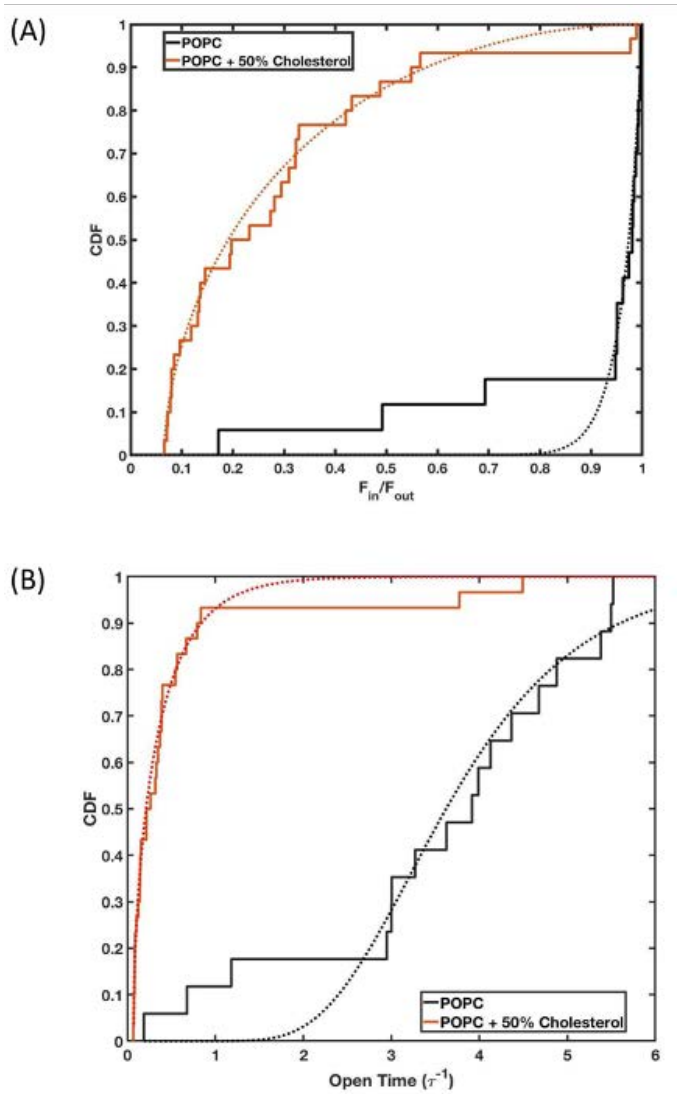

Figure S1. Effect of cholesterol on fusion peptide induced pores. (A) Cumulative distribution functions (CDF) of the extent of influx ($R = F_{in}/F_{out}$) for POPC and POPC + 50% cholesterol GUV are described by generalized Kumaraswamy distributions: (CDF = $1 - (1 - z^{\alpha})^{\beta}$; $z = (R - R_{\min})/(1 - R_{\min})$). (B) Cumulative distribution functions for the influx time for POPC in the presence and absence of cholesterol following remapping of R onto the general kinetic relationship $R = (1 - e^{-t/\tau})$ where τ is a characteristic time constant for the influx process. The cumulative distribution functions for the open time for POPC, as a function of time in units of τ, in the presence and absence of cholesterol are described by generalized exponential distributions (CDF = $(1 - e^{(-\lambda(t/\tau - (t/\tau)_{\min}))})^{\alpha}$) with location ($(t/\tau)_{\min}$), shape ($\alpha$), and scale ($1/\lambda$) parameters.

Aggregation Analysis

In the absence of peptide aggregation, the naïve expectation is that spatial distributions are random, and that the membrane of a GUV with sufficiently bound peptide, visualized in a cross-section with an approximately circular shape, would have uniform intensity along the circumference of the ring parameterized by the radial angle. However, even if a chromophore is uniformly bound to the surface with identical orientations on the surface, the polarization properties of a high NA objective will lead to a cosine-squared dependent modulation of the otherwise constant intensity[1-3]. The intensity profiles in our experiments were calculated following template matching alignment (to minimize position jitter noise), using the ImageJ plugins (Template Matching and Oval Profile Plot); Figure 2A. Unlike the profiles predicted for a chromophore uniformly bound to the surface with identical orientations on the surface, the observed profiles at a single time point or averaged over a subset of time points (5, for example) or the entire time series could not be described using either a single uniform orientation or two component mixtures of orientations. Since the goal is to identify pixels with larger than expected intensity (a statistical evaluation), both the slowly varying modulation around the circumference and the magnitude of the intensity must be considered since the variance increases with intensity. Our hypothesis predicts that higher than expected concentrations of bound peptide are present during the process of poration; the analysis first calculates the intensity surface at the time of poration followed by an analysis of the distributional properties of the residuals; the maximum intensity pixel on the GUV is compared to those obtained in solution using extreme value theory[4]. Direct calibration issues were avoided by normalizing the GUV pixel intensities into units of solution intensity calculated from the distribution of intensities along a 1-pixel wide ring matching the size of a GUV in cross-section. Since the distributions of peptide intensity in solution, over time, often captured transient, peptide bound membrane structures, the distributions were modeled as a two component Gaussian mixture, with the lower intensity mean taken as the peptide intensity in solution to be used in the normalization of membrane bound peptide. It is possible that the properties of the chromophore change following peptide binding to the membrane. However, this behavior was not observed because the initial normalized GUV intensity is approximately 1 (Figure S2B; solid horizontal line at ~ 1 for normalized GUV intensity values less than t_{crit} = 147 sec). Consequently, the intensity on the GUV surface is expressed in units of solution intensity that is directly related to the peptide concentrations used.

Figure S2B compares the peptide in solution and bound to the GUV, expressed in units of the mean intensity measured in solution and averaged over the circumference of a ring with the same diameter as that of the confocal image of the GUV. Note, the solution values are invariant with time while there is a time at which the intensity of the peptide bound to the GUV begins to diverge and increase with time. The extent of Alexa 488 influx ($R = F_{in}/F_{out}$; green trace) is also plotted and the time of poration indicated by the red arrow. The characteristic time for poration, represented by the difference between the time leakage is first detected and the time the normalized peptide fluorescence on the vesicles increased above the peptide fluorescence in solution, and solution normalized peptide density are, 101 +/- 22 sec, and 2.7 +/- 0.05, (mean +/- SEM; n = 9), both log-normally distributed.

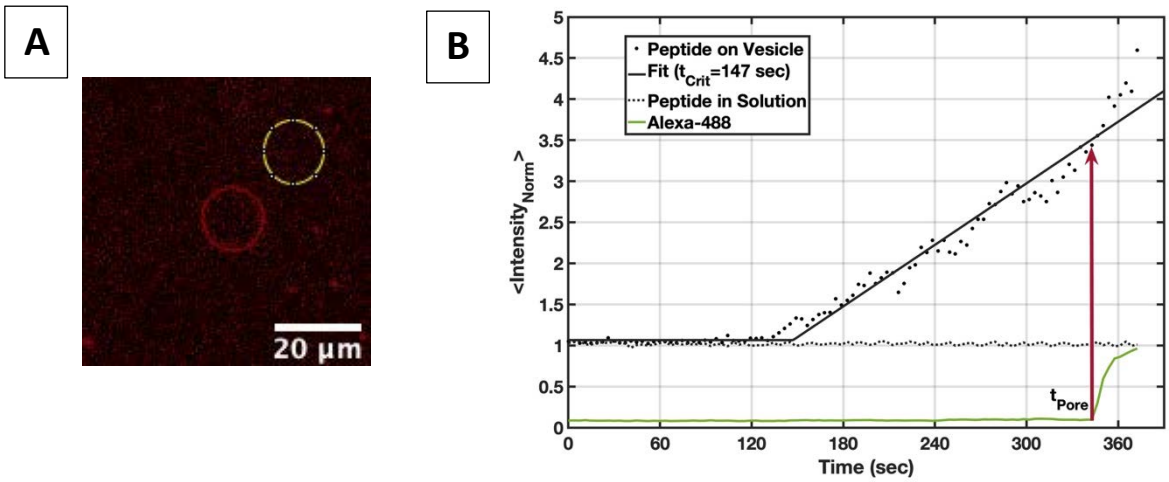

Figure S2. Kinetics of poration and peptide accumulation on a POPC GUV. A) Confocal image of peptide labeled vesicle (red) and ring (yellow), positioned in the solution, used to evaluate circumferential intensity of both the vesicle and solution as a function of time. B) The peptide fluorescence signal was normalized by the peptide mean intensity in solution and the time when peptide begins to accumulate on the vesicle, t_{Crit}, determined using piecewise linear fitting. The time, t_{Pore}, when poration begins (red arrow) was determined using piecewise linear and exponential fitting. In this example, the characteristic time between peptide accumulation and poration is 197 sec with a mean peptide intensity at poration 3.5 times the solution intensity.

A window +/- 2 timepoints around the estimated poration time, t_{Pore}, was analyzed for the presence of pixels having larger and smaller than expected peptide intensity. The data, defined by 3 parameters (radial angle, time, pixel intensity) was first fit, for the peptide in solution, with a plane surface while for the peptide bound on the vesicle the angle dependent modulation was removed by subtracting a spline smoothed circumferential mean (over the five time points) to remove any large scale (quadrant angle level) polarization dependent intensity modulation of peptide bound to the vesicle (Figure S3). The resulting deviations (residuals), following adjustment by the square root of the mean intensity (to adjust for the known magnitude scaling of a random variable) are compared to the distributional behavior of peptide in solution. The residuals represent both the positive and negative deviations around the mean; larger (smaller) than expected intensity deviations on the vesicle, when compared to the solution distribution that is known to be consistent with a randomly oriented, uniform intensity distribution, are evidence for pixels with greater (lower) peptide density. The spatial distribution of the peptide intensities in solution represents the expected variation for orientationally random and spatially uniformly distributed data since the surface was 1) described by a plane at a constant value of 1 (the normalized intensity) and 2) the residuals were symmetric around 0, and well described by a zero mean Gaussian. However, the residuals for the peptide on the vesicle were broader with extended tails, relative to the solution distribution, indicating that many pixels have higher than expected intensities under the hypothesis that the distribution of peptide on the vesicle is just a

scaled version of the observed uniform distribution in solution; this observation is consistent with aggregation of peptide at the pixel level.

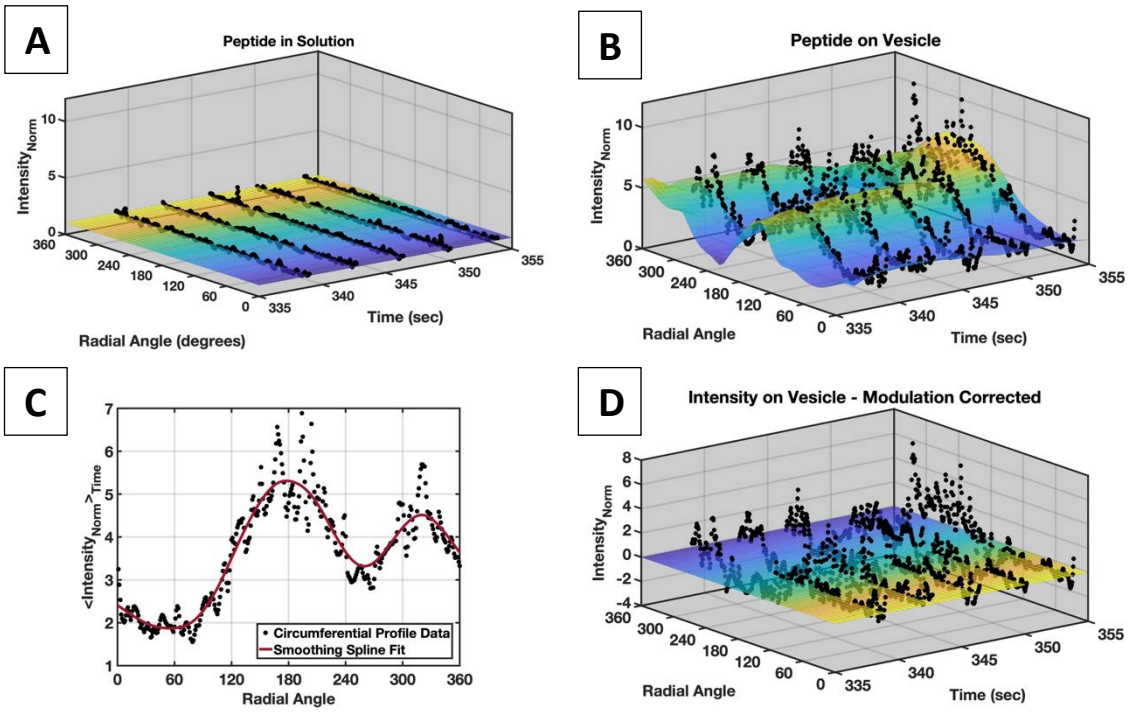

Figure S3: Circumferential pixel intensity in a time window around the time of poration, t_{Pore} = ~ 344 sec. (A) In solution, the intensity is constant both in time and along the circumference while in (B) the intensity on the vesicle is noisy and modulated. The surface shown was calculated using locally weighted, smoothing quadratic regression (Lowess quadratic) using a data span of 20% to demonstrate the complexity of the time, angle, intensity surface. (C) shows the mean circumferential intensity, as a function of radial angle, and the smoothing spline fit that was used to characterize the hypothesized, polarization dependent modulation of the circumferential intensity. The intensity variations observed in (B) were evaluated around this smoothing curve, effectively removing the large-scale modulation, and are shown in (D) where the resulting deviations are fit by a plane at the intensity origin. The maximal positive values were then assigned probabilities based on the distribution of residuals observed in (A) following a correction for the magnitude of the intensity. This correction removes the known and expected scaling of the variance with mean intensity where in the simplest case, Poisson statistics, the variance equals the mean.

We applied Extreme Value Theory to evaluate whether maximum(minimum) vesicle pixel intensities arise from a uniformly distributed peptide density on the vesicle using the pixel intensity distributions observed in solution that are known to be uniformly distributed. The rationale of an extreme value approach is that the deviations associated with “extreme” (maximal or minimum) pixels should be much larger than those deviations calculated for the

peptide in solution where the solution distribution is best described as orientationally random and spatially uniformly distributed. The goal is to assign a probability to the peptide bound, pixel intensity using the distribution describing the solution pixels. If this probability is very low, then we have confidence that the vesicle pixel is not a member of the solution pixel intensity distribution, and it is appropriate to identify this pixel as an outlier whose value is greater (lesser) than expected. However, traditional measures (multiple standard deviations, for example) are not applicable because they do not accurately describe the tails of distributions. Extreme Value Theory was used to estimate the distribution of the tail of the solution data to both estimate the probability and test the hypothesis that the intensity of the maximal vesicle pixels are members of the solution distribution. The subsequent analysis compares the statistical probability that the largest (smallest) normalized deviation observed on a vesicle could have resulted from the expected variation observed in solution. Low probability (less than 0.01, for example) suggests that the value is unlikely to have been the result of a random fluctuation of the intensities represented in solution and is consistent with the hypothesis that these values are much greater (lower) than expected and therefore, consistent with a greater (lower) peptide density then that which can occur if the peptide bound to the surface of the vesicle was orientationally random and spatially uniformly distributed.

The residual distributions for both peptide in solution and bound to a vesicle are shown in Figure S4. In solution, the peptide intensity deviations around the normalized mean are described by a zero mean Gaussian with only a few deviations up to a value of 1; a value of 1 represents a doubling of the normalized intensity. However, when bound to the vesicle, the peptide deviations are significantly right (left) shifted corresponding to pixel intensity values that are greater (lesser) than observed for a known distribution that is orientationally random and spatially homogeneous. Again, these observations are consistent with a non-homogeneous spatial distribution of peptide on the surface of the vesicle with some areas having greater or lesser peptide density than that expected from a uniform distribution even after correcting for variations in the mean intensity and polarization dependent modulation of the intensity signal along the circumference.

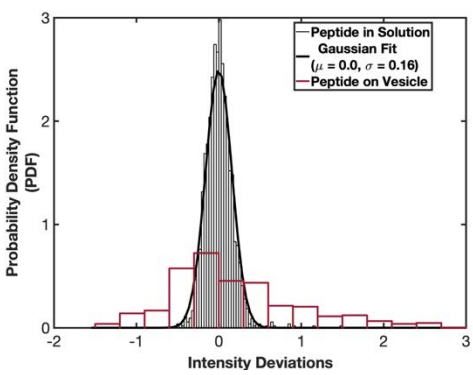

Figure S4: Distributions of the pixel intensity deviations for peptide in solution and bound to the vesicle. The intensity distribution in solution is described by a zero mean Gaussian (μ) with standard deviation σ while the intensity distribution for the bound peptide has many examples that are much greater than observed in solution.

The limiting behavior of the solution residuals distribution was evaluated using the Generalized Pareto distribution (GPD) implemented in the MATLAB (MathWorks; Natick, MA) command paretotails. This distribution captures the three extreme or asymptotic behaviors (short, long,

and exponentially tailed) of data distributions depending upon the threshold, scale, and shape parameters. However, since the distribution captures the asymptotic behavior of the data, the selection of the threshold point is critical: too low a threshold leads to characterizing a distribution that is a mixture of the extreme part and the average, too high gives insufficient numbers of extreme values or exceedances to characterize the distribution. We focused on the positive tail of the residual distribution, specifically examining pixels with higher-than-expected intensities (peptide densities), and the tail distribution was modeled with a range of residuals that included all the positive data to the 25 most extreme data points. In this example, the tails were first evaluated using an extreme value threshold corresponding to the positive 95% confidence of the Gaussian distribution that describes the solution distribution and then a range of thresholds were considered (Figure S5). Rather than assigning a single probability from a selected extreme value calculation, a range is reported corresponding to the upper limit (based on the 95% confidence threshold; Figure S5A) and a lower limit based on a less conservative threshold value (Figure S5B). Using a conservative threshold in which the GPD is calculated at an intensity deviation of 0.32, corresponding to a 95% confidence level in the Gaussian estimate of the solution intensity distribution, there are peptide intensity deviations on the vesicle that have less than a 0.01 probability of arising from the expected fluctuations in solution. The intersection of the fit (dotted line) and the probability p = 0.01 (green line) indicates that and intensity deviation greater than ~ 2.3 has a probability lower than 1% of being described by the solution distribution. The number of peptide-bound intensity deviations greater than this cutoff is represented by the red line and corresponds to a total of 43 pixels with peptide intensities greater than expected and represent potential sites of peptide aggregation. A less conservative threshold (0.25 compared to 0.32), based on the behaviors of the scale and shape fitting parameters shifts the intersection from ~2.3 to 1.5 and increases the number to over 100 pixels with greater than expected peptide intensities (Figure S5B). Since our goal is to demonstrate that the characteristics of the distribution of bound peptide are not orientationally random and spatially homogeneous, we considered the tail behavior

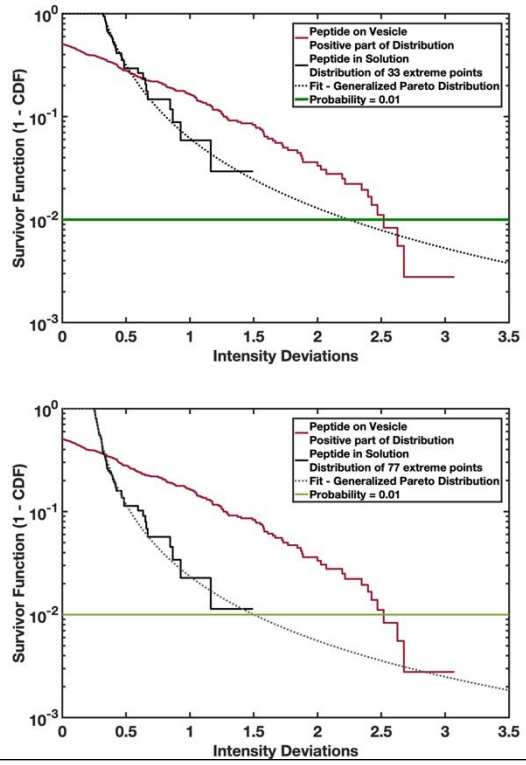

Figure S5: Extreme value analysis using two different thresholds. (A) GPD analysis using 33 extreme data points in the solution distribution based on the cutoff determined from the Gaussian distribution. ~ 40 peptide bound pixel intensities with deviations greater than ~2.3 have a low probability (less than 0.01) of arising from fluctuations expected in solution. (B) A less conservative threshold shifts the cutoff value to 1.5 and increase the number to over 100 pixels with greater than expected peptide intensities at p = 0.01.

calculated at threshold values represented using both a 90% and 95% cutoff corresponding to evaluating the GPD with either 10% (180 data points) or 5% (90 data points) of the positive tail. Using the 90% cutoff, 8 of 9 experiments demonstrated pixels that have higher than expected intensity deviations: the number of pixels ranged from 3 to 269 ($p = 0.05$ level) with the maximal probabilities of the highest pixels ranging from <0.0001 to 0.049. Using the 95% cutoff, 7 of 9 experiments demonstrated pixels that have higher than expected intensity deviations: the number of pixels ranged from 10 to 179 ($p = 0.05$ level) with the maximal probabilities of the highest pixels ranging from <0.0001 to 0.0065.

The pixels with higher-than-expected peptide intensities are ~ 10 times greater than the average intensity in solution. A rough estimate of the number of peptides is possible since the Peptide:Lipid ratio was constant for all experiments as was the starting concentration of both the Lipid and Peptide (0.6 mM and 3 μM, respectively). With a nominal voxel size of 1x1x2 μm^3 and all peptides in the voxel contributing to the intensity measured in a nominal 1x1 μm^2 pixel, a rough estimate of the number of peptides present at these "hot spots" is ~ 36,000. Assuming a uniform distribution at the level of a single voxel, the number of peptides, when scaled to the size of the MD simulation (15 nm x 15 nm) is approximately 8; a value that is consistent with MD modeling suggesting that aggregates of the appropriate number are present in our experimental system in these regions that are not spatially homogeneous.

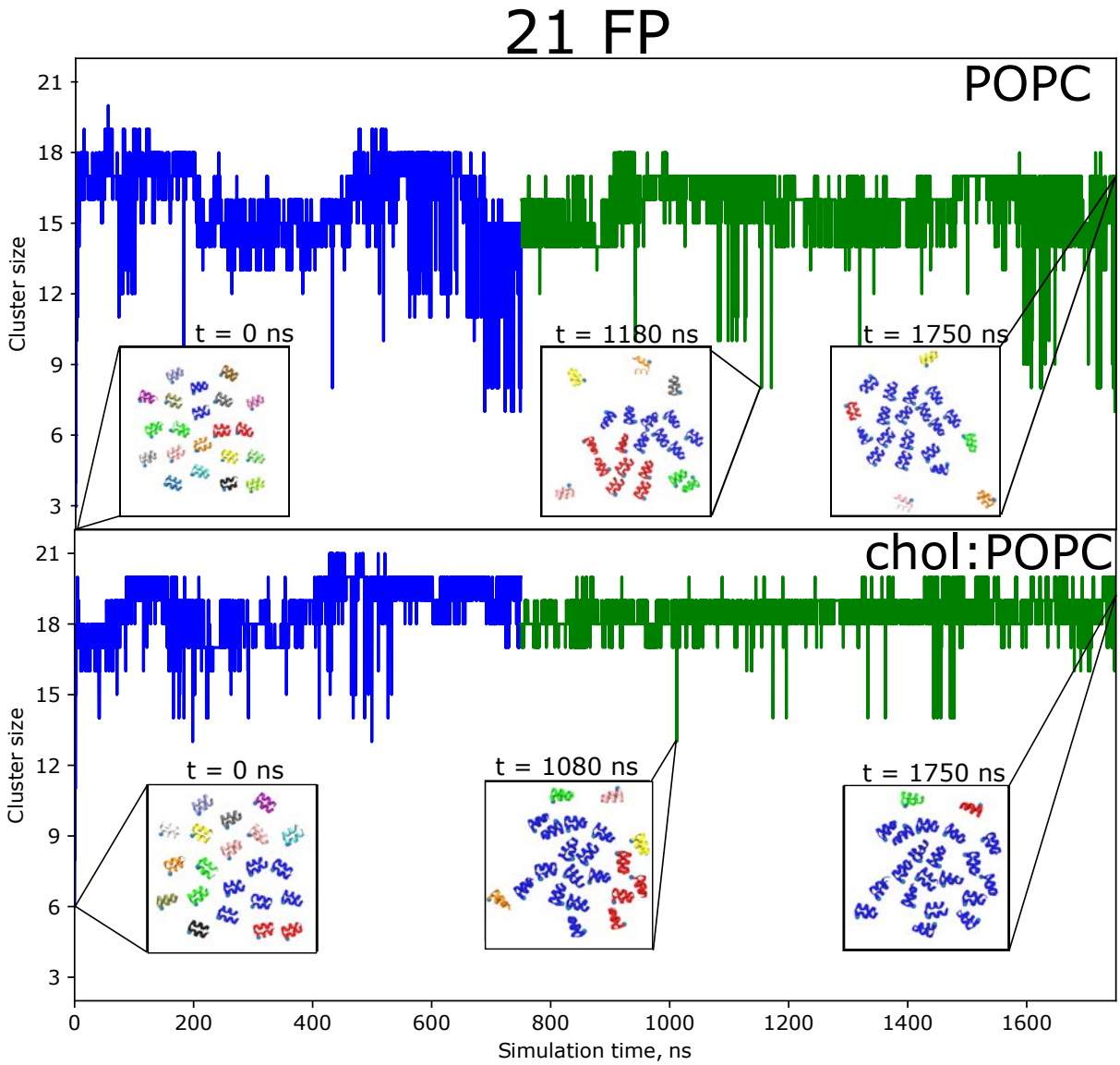

Figure S6. Largest peptide cluster size as a function of simulation time for POPC (top) and chol:POPC (bottom) membranes. Data for 21 FP systems. Clustering based off all peptide heavy atoms. Insets show snapshots from the simulation, with peptides colored based on which cluster they are assigned to. The largest three clusters are always denoted by blue, red, and green peptides respectively.

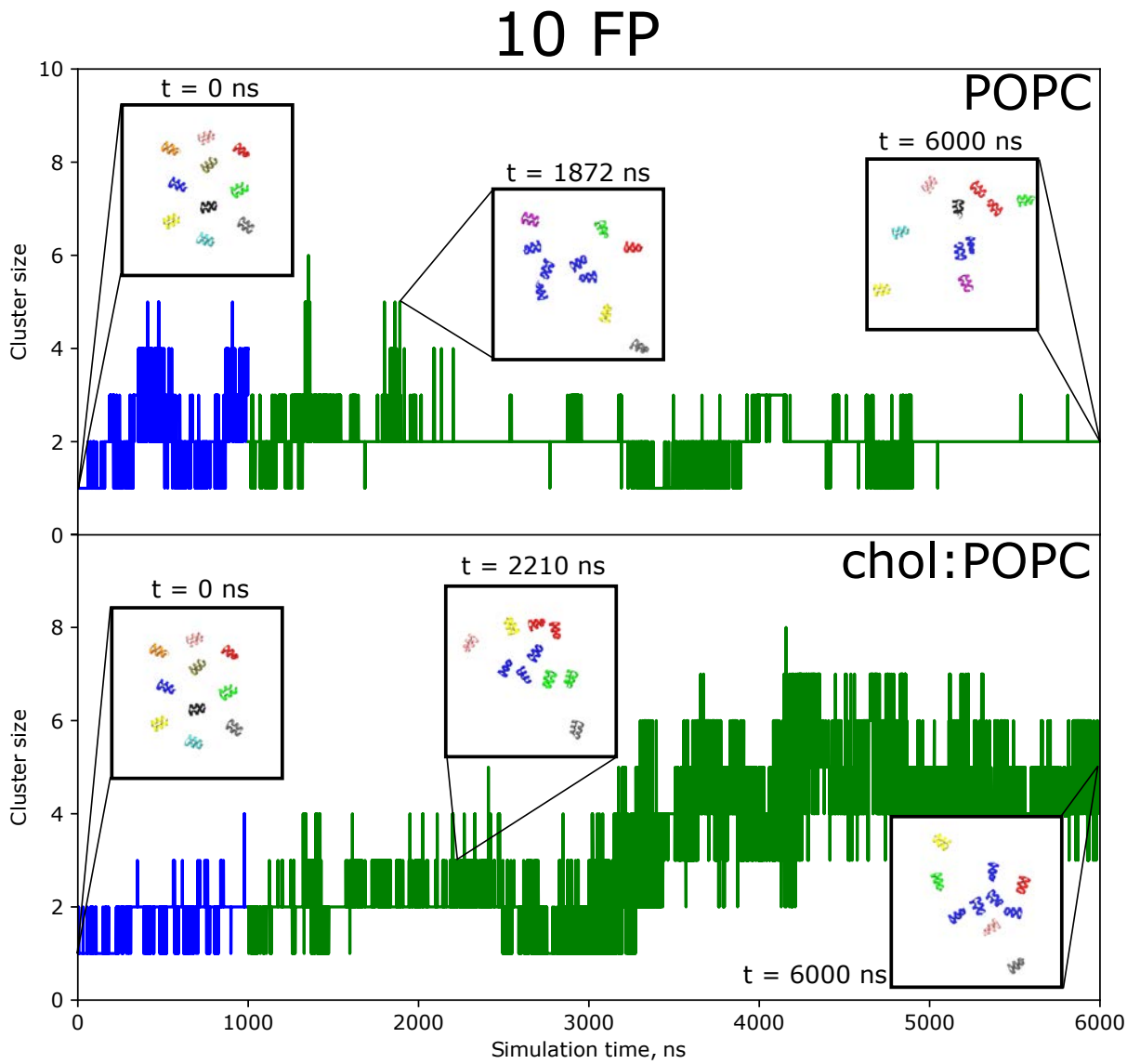

Figure S7. Largest peptide cluster size as a function of simulation time for POPC (top) and chol:POPC (bottom) membranes. Data for 10 FP systems. Clustering based off all peptide heavy atoms. Insets show snapshots from the simulation, with peptides colored based on which cluster they are assigned to. The largest three clusters are always denoted by blue, red, and green peptides respectively.

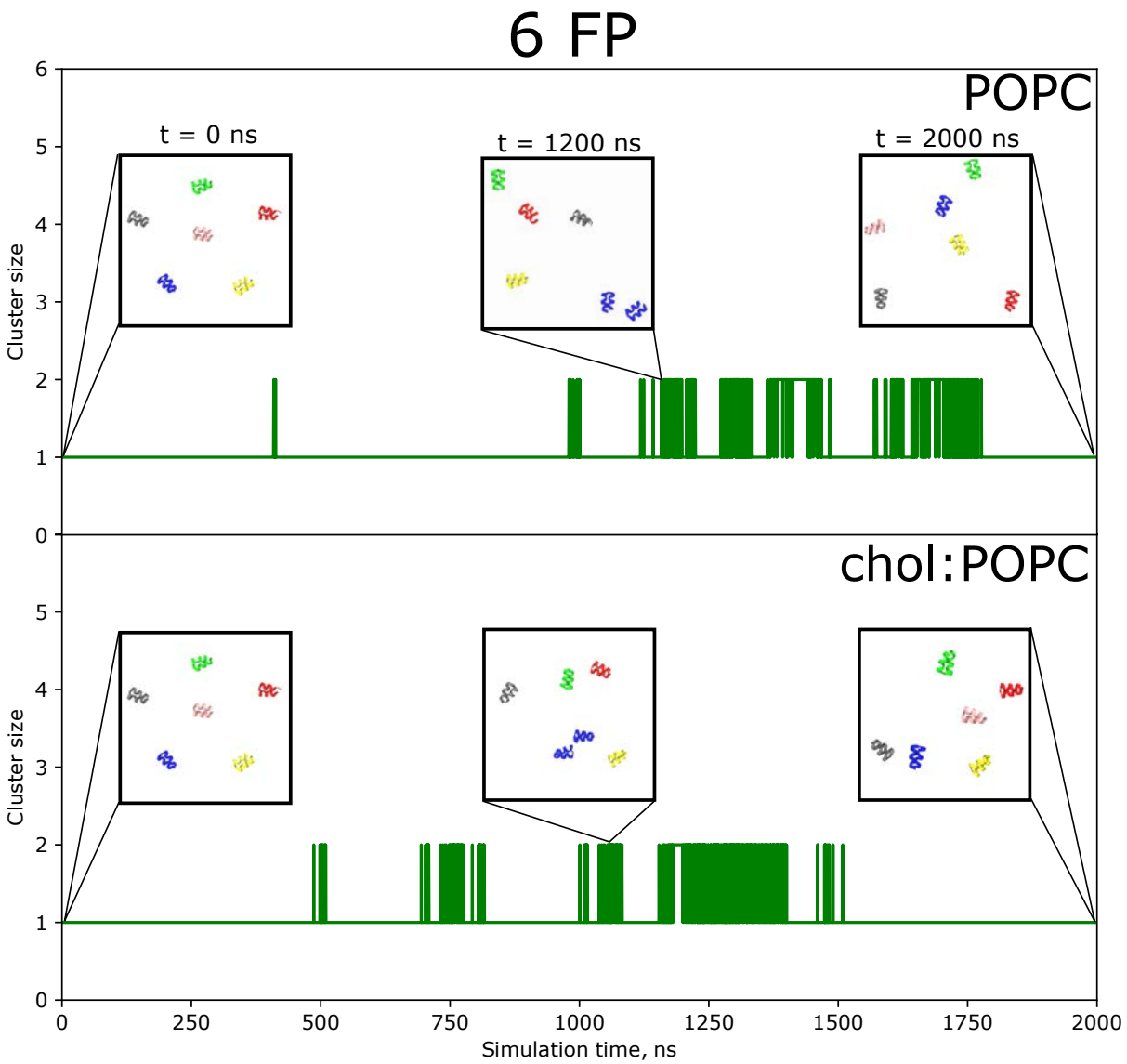

Figure S8. Largest peptide cluster size as a function of simulation time for POPC (top) and chol:POPC (bottom) membranes. Data for 6 FP systems. Clustering based off all peptide heavy atoms. Insets show snapshots from the simulation, with peptides colored based on which cluster they are assigned to. The largest three clusters are always denoted by blue, red, and green peptides respectively.

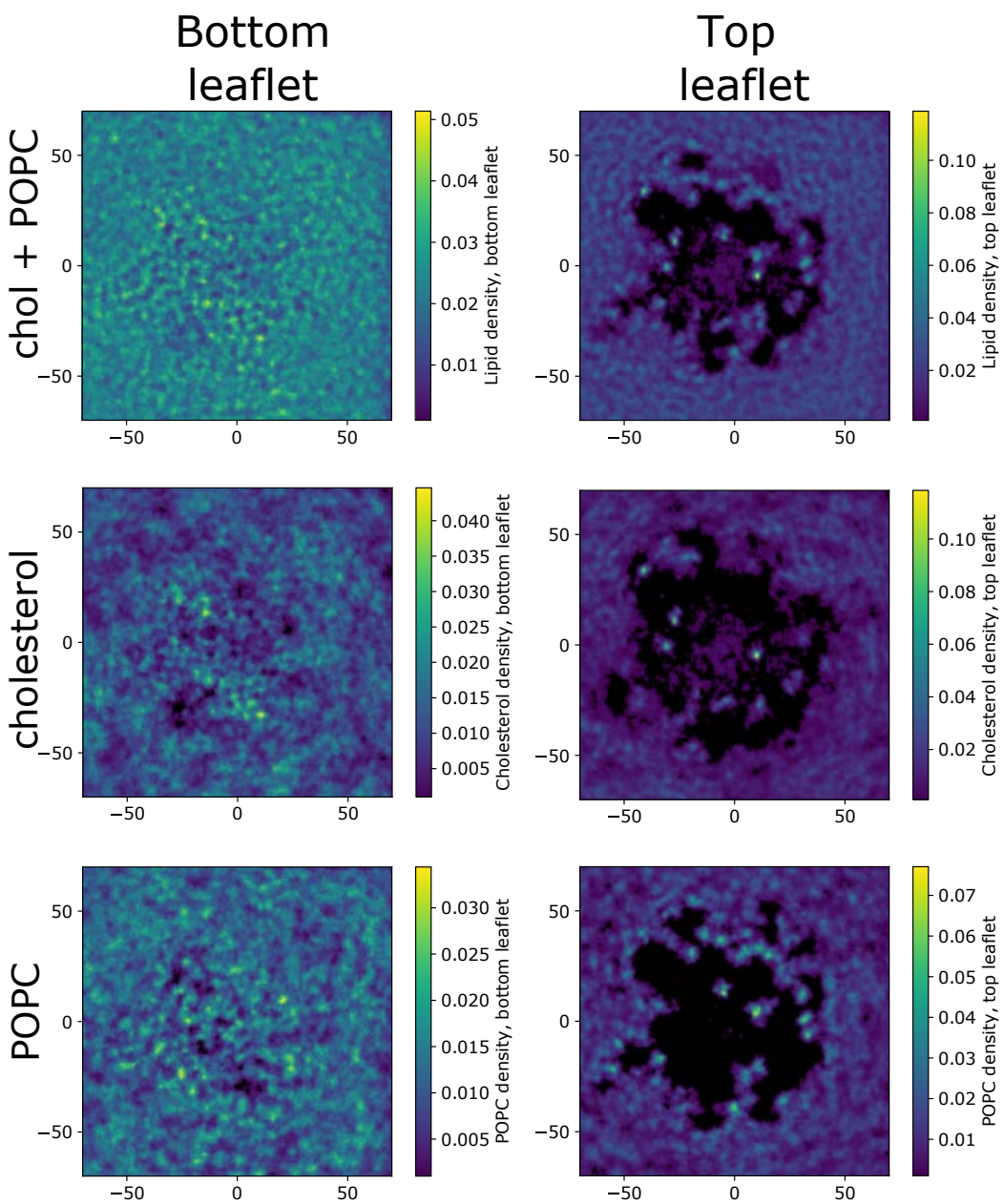

Figure S9. Lipid number density maps of the chol:POPC:21FP system. Number density plots are shown for individual lipid components (cholesterol and POPC) as well as all lipid components. The region devoid of lipids in the upper leaflet is where the peptide aggregate is centered.

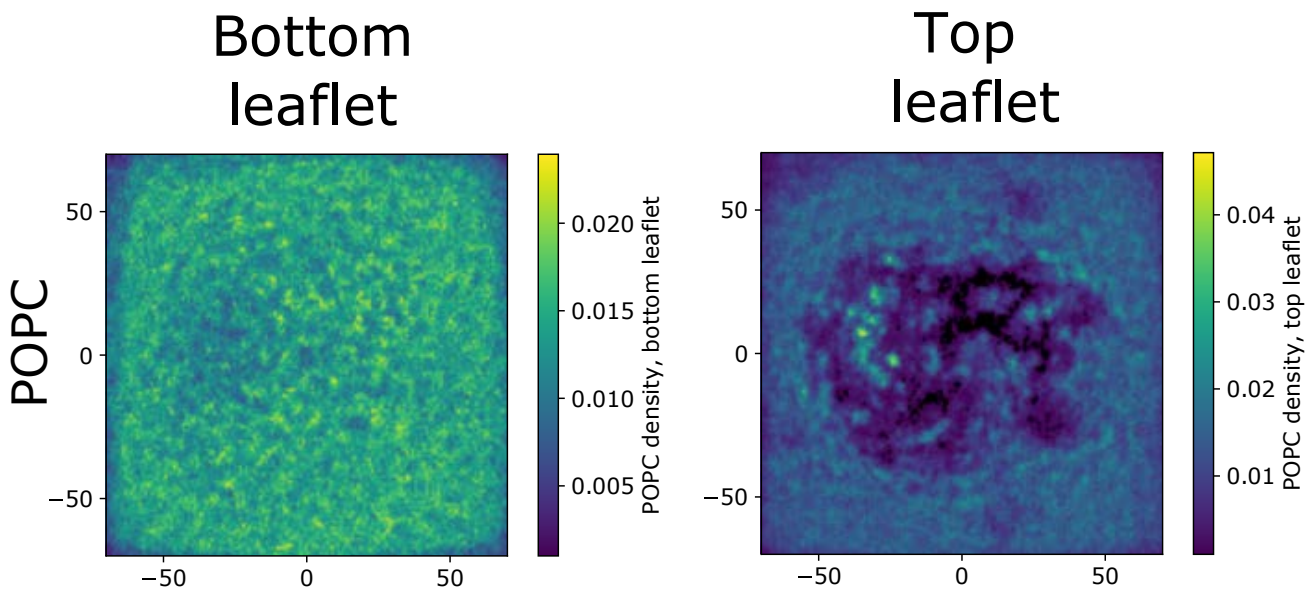

Figure S10. Lipid number density maps of the POPC:21FP system. Number density plots are shown for both leaflets. The region devoid of lipids in the upper leaflet is where the peptide aggregate is centered.

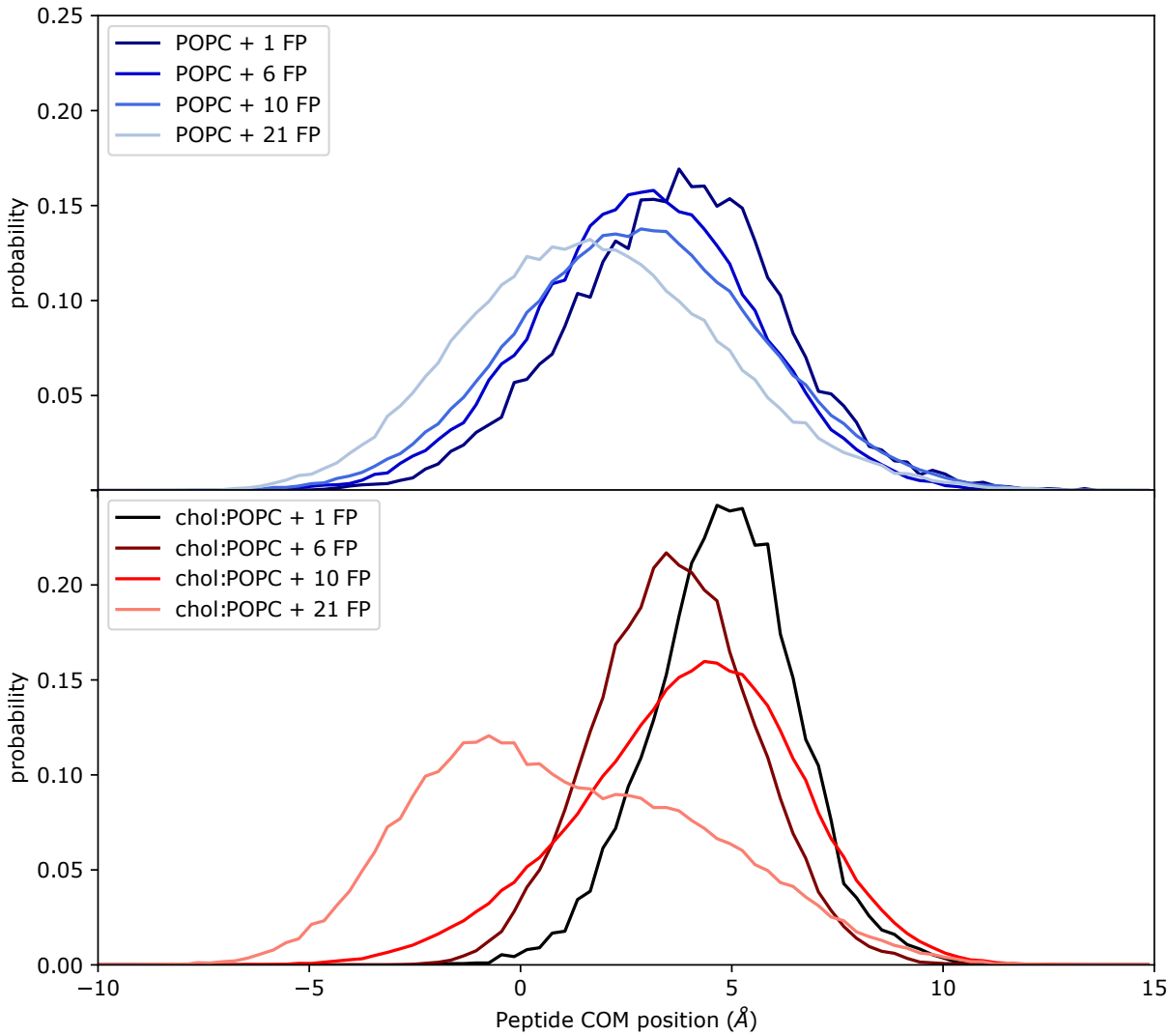

Figure S11. Peptide center of mass location. Probability distributions of the peptide center of mass location with respect to the POPC C2 plane for the pure POPC (top panel) and chol:POPC (bottom panel) systems. The peptide aggregates insert more deeply than the isolated peptide, regardless of the bilayer composition.

# of FP	POPC Thickness (Å)	chol:POPC thickness (Å)
0	27.5 ± 0.3	34.5 ± 0.3
1	26.5 ± 0.3	34.0 ± 0.2
6	26.0 ± 0.3	33.0 ± 0.2
10	25.5 ± 0.3	30.0 ± 0.2
21	19.0 ± 0.4	21.5 ± 0.3

Table S1. Bilayer hydrophobic thickness for asymmetric bilayers. Distance is measured from the C2 density distribution profiles as the distance between the two peaks. C2 density is only calculated over the portion of the trajectory within a cylinder of radius 30 Å centered at the origin (Figure S14).

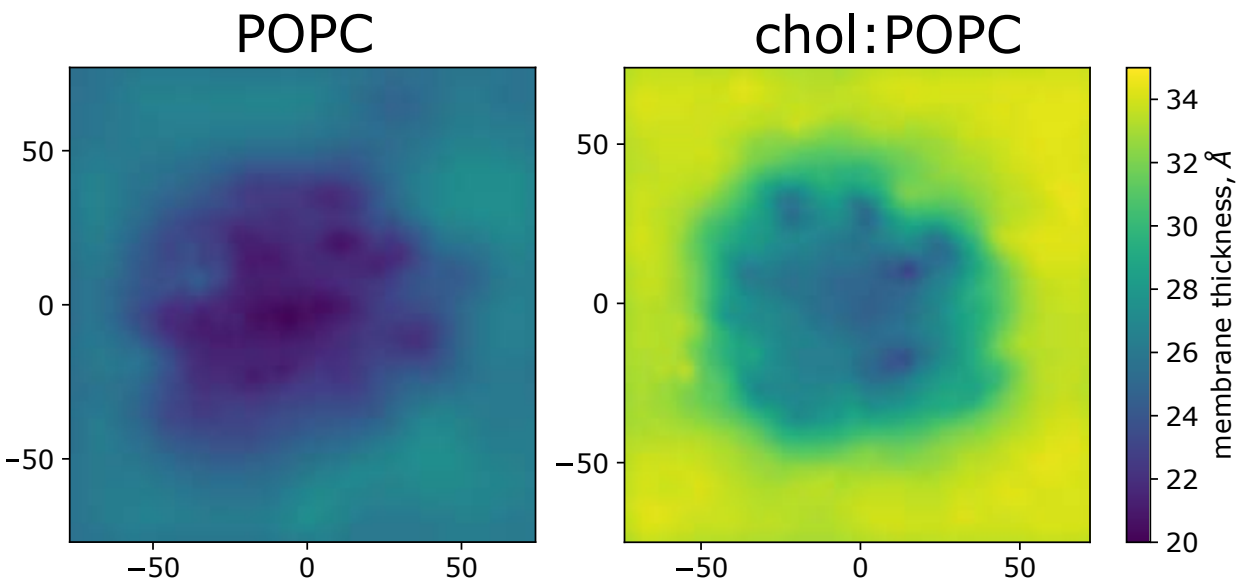

F**igure S12. Membrane thickness maps**. Membrane C2-C2 thickness maps for the POPC:21FP (left) and chol:POPC:21FP (right) systems. The fusion peptide aggregate has been centered at the origin for both systems.

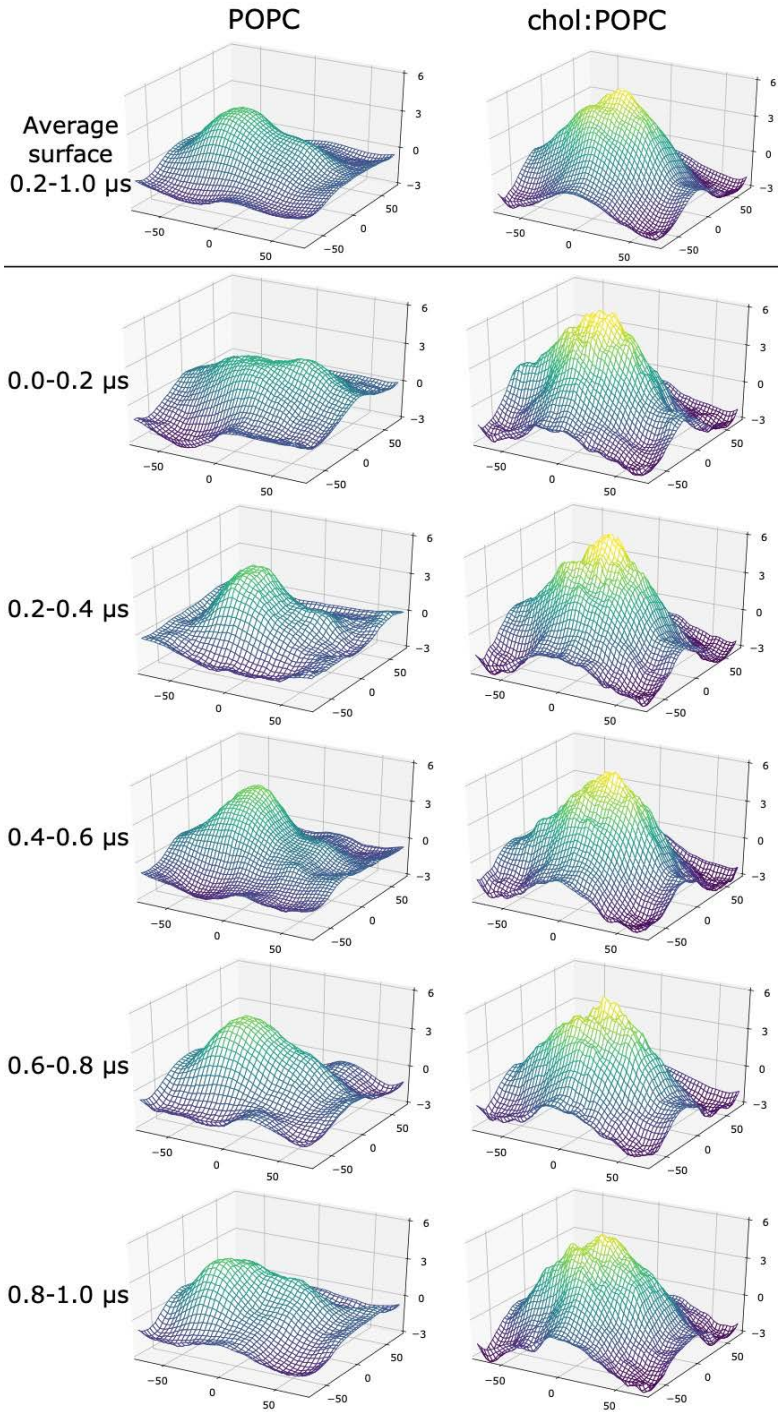

Figure S13. Bottom leaflet curvature in 21 FP simulations. Bottom leaflet surface plots for the POPC:21FP (left) and chol:POPC:21FP (right) systems, calculated over 200 ns portions of the simulation. Z = 0 has been set to the average position of all POPC C2 atoms in the leaflet.

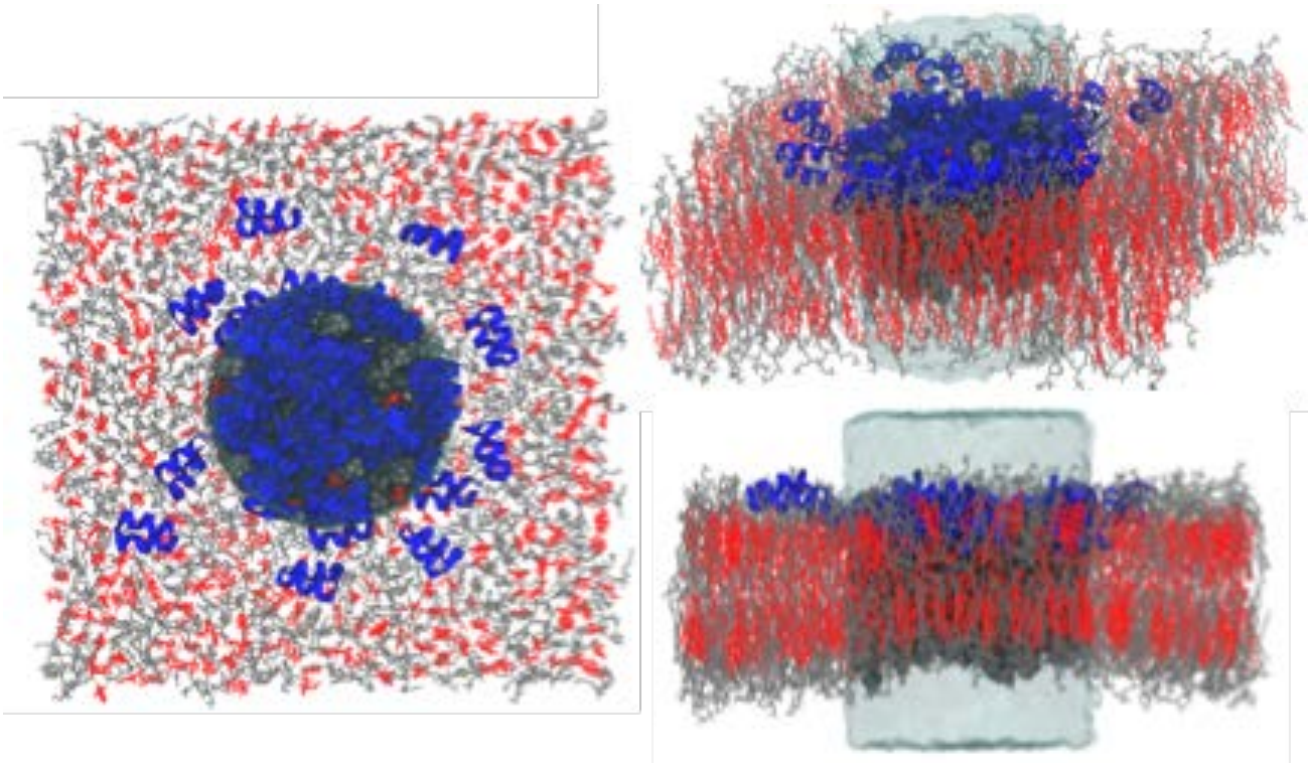

Figure S14. Visualization of the cylindrical region used for density profile calculations. Molecules within the cylinder, with radius 30 Å centered at the origin, are depicted in a space-filling representation, while the water within the cylinder is depicted as a transparent bubble. POPC and cholesterol are shown in grey and red, respectively; peptides are in blue; water outside the cylinder is not shown.

System	$1/\bar{R}$ (Å^{-1})	Water-wire energy (kcal/mol)	Normalized hydrophobic defect energy (kcal/mol)
		POPC Bilayer	
POPC	382 ± 38	39.1 ± 0.6	22.3 ± 0.6
POPC : 1 FP	611 ± 16	36.0 ± 0.2	20.5 ± 0.2
POPC : 6 FP	850 ± 56	34.7 ± 0.2	19.8 ± 0.2
POPC : 10 FP	1940 ± 275	31.4 ± 0.3	17.9 ± 0.3
POPC : 21FP	3559 ± 483	26.2 ± 0.3	14.9 ± 0.3
		POPC:Chol Bilayer	
chol : POPC	68 ± 14	65.5 ± 0.8	37.3 ± 0.8
chol : POPC : 1 FP	63 ± 4	64.4 ± 0.5	36.7 ± 0.5
chol : POPC : 6 FP	42 ± 4	60.9 ± 0.2	34.7 ± 0.2
chol : POPC : 10 FP	240 ± 41	43.5 ± 0.9	24.8 ± 0.9
chol : POPC : 21FP	137 ± 51	34.0 ± 0.3	19.4 ± 0.3
		POPC Trans Leaflet	
POPC	764 ± 80	19.0 ± 0.6	11.1 ± 0.6
POPC – across from 1 FP	1302 ± 35	17.7 ± 0.2	10.4 ± 0.2
POPC – across from 6 FP	1715 ± 393	17.0 ± 0.2	9.9 ± 0.2
POPC – across from 10 FP	4291 ± 643	15.2 ± 0.3	8.9 ± 0.3
POPC – across from 21 FP	8018 ± 351	11.4 ± 0.3	6.7 ± 0.3
		POPC:Chol Trans Leaflet	
chol:POPC	137 ± 28	32.3 ± 0.8	18.9 ± 0.8
chol:POPC – across from 1 FP	117 ± 2	32.3 ± 0.5	18.9 ± 0.5
chol:POPC – across from 6 FP	55 ± 11	30.8 ± 0.2	18.0 ± 0.2
chol:POPC – across from 10 FP	378 ± 50	23.5 ± 0.9	13.8 ± 0.9
chol:POPC – across from 21 FP	179 ± 43	16.7 ± 0.3	9.8 ± 0.3

Table S2. Resistances to permeability, $\bar{R}$, Water-wire energy, and 1.3-nm hydrophobic defect energy, representing the barrier towards pore formation. $\bar{R}$ for all systems were calculated within the 30 Å radius cylinder shown in Figure S11.

Molecular Dynamics Simulations with an Applied Electric Field

POPC bilayers with 0 and 50% cholesterol with FPs were assembled and an electric field was introduced after the systems were equilibrated. Surface views of the POPC and chol:POPC systems in the absence and presence of an electric field are shown in Figure S152A. A detailed snapshot of a pore in POPC formed with an electric field is shown in Figure S15B. The total area (X·Y) as a function of time is reported in Figure S15C, which illustrates the expansion of the pore due to the electric field. The 1.2 V field creates notable pore expansion in the POPC system (Fig. S15C*i*) but does not lead to significant increases in the chol:POPC system within the 9 ns simulation time (Fig. S15C*ii*). Therefore, the chol:POPC membrane is more resistant to electric field induced poration. It is possible that longer exposure to the electric field would create pores in chol:POPC; replicate 2 appears to undergo some increase in surface area from 8-9 ns. However, longer simulations produce excessive bilayer expansion in the pure POPC membranes, which ultimately leads to simulation error. Since the 1.2 V field does not create pores within the simulation time, the kinetics of pore formation cannot be probed. To address this problem, the field strength was increased to 1.4 V such that pores would be created in all systems. From visual inspection, there is a delay in pore formation in the chol:POPC membrane relative to the POPC membrane (Fig. S15C *iii* and *iv*). Defining a threshold area of 256 nm^2 = $(16\ nm)^2$, the time to reach this threshold area is 2.1 ± 0.3 ns for POPC and 3.7 ± 0.4 ns for chol:POPC (mean ± SEM; n = 5), which represents a significant delay in the presence of cholesterol (t-test p = 0.015). A distinct physical event that can be used to follow pore formation is the initial formation of a water wire, which is determined by visual inspection of the simulation trajectories as shown in Figure S16. The average time to form the displayed wires are 0.9 ± 0.4 ns for POPC and 2.3 ± 0.4 ns for chol:POPC (mean ± SEM; n = 5) at an applied voltage of 1.4 V. As with the surface area plots, chol:POPC displays a significant delay relative to POPC (equal variance, unpaired, T-test, p = 0.033). However, referencing the wire formation time against Figure S15, wire formation is within the initial plateau region and therefore not discernible from the surface area. Furthermore, visual inspection reveals a structural difference between the POPC and chol:POPC water files that are formed. While chol:POPC membranes show straight single-file lines of water, which is the general

model of a water wire, the POPC membranes form larger extensions that eventually connect the top and bottom water layers (in replicates 2-5 of the POPC calculation, Fig. S16).

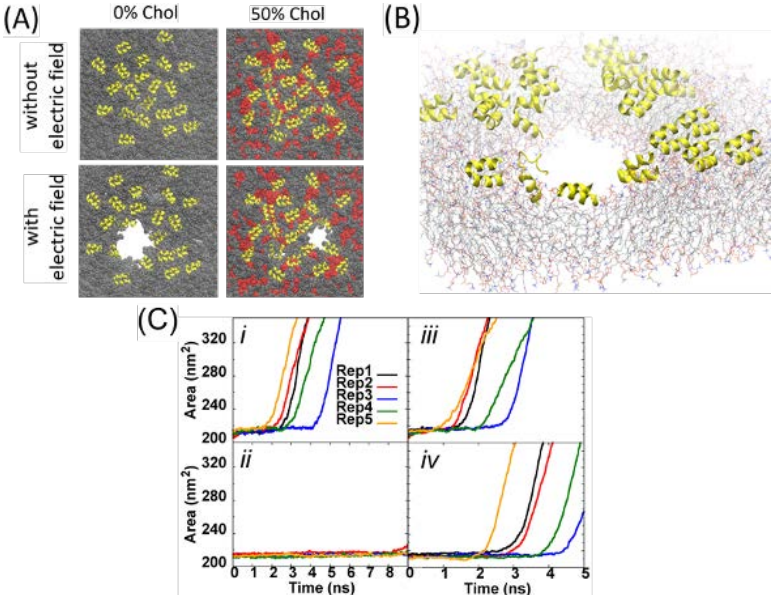

Figure S15. Formation of pores in electric field simulations. (A) Snapshots of the simulations systems in the absence (top row) and presence (bottom row) of an applied electric field. Coloring is as follows: POPC, gray; cholesterol, red; peptides, yellow. (B) A detailed snapshot of a pore in POPC formed with an electric field. (C) Total surface area of the simulation box as a function of time. (*i*) represents POPC with a 1.2 V field, (*ii*) represents chol:POPC with a 1.2 V field, (*iii*) represents POPC with a 1.4 V field, and (*iv*) represents chol:POPC with a 1.4 V field.

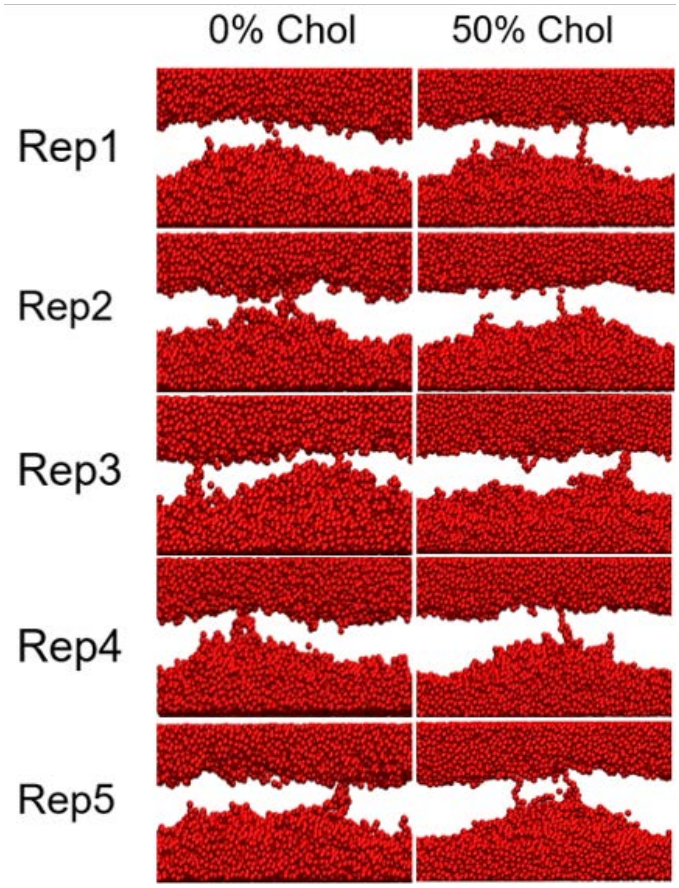

Figure S16. Pore formation in simulations in the presence of a 1.4 V electric field. Snapshots from simulations showing water wire formation. Water is shown in red; lipids and peptides are omitted for clarity.

Formation of the peptide cluster.

The energy of the *N* isolated FPs is: $E_{FP0} = NE_{FP}$, where E_{FP} is the energy of a single FP, arising, for example, from peptide-induced deformations of the membrane. Energy of a cluster of radius *R* is stored in its boundary: $E_{cluster} = 2\pi R\gamma(R)$, where γ is the cluster line tension. Dependence of the line tension of the cluster on its radius is presented in figure S17. The dependence is obtained as an elastic energy of the membrane induced by the cluster boundary divided by its perimeter. The elastic energy arises upon compensation of the thickness mismatch at the cluster boundary, as the bilayer membrane and the "hybrid" peptide-lipid bilayer of the cluster have different thicknesses.

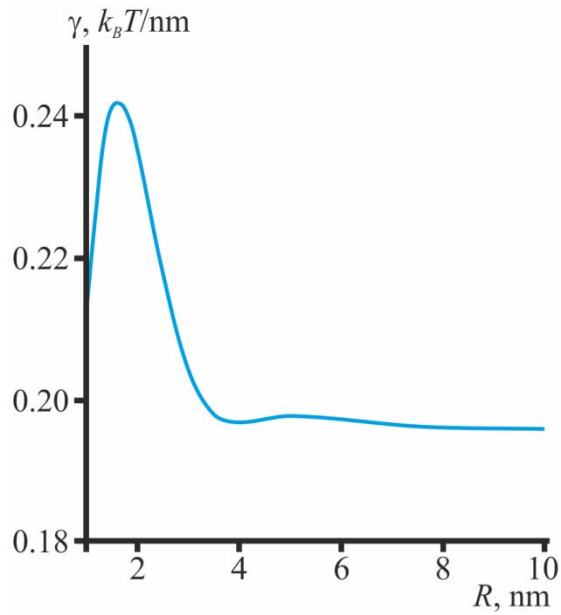

Figure S17. Dependence of the line tension of the cluster on its radius. FP monolayer thickness in taken to be equal to h_{FP} = 1.1 nm, surrounding membrane thickness h = 1.5 nm.

The radius of the cluster can be related to the number of FP in the cluster:

$$R = \sqrt{\frac{n_{clust} a_0}{\pi}} \tag{S1}$$

where a_0 is the lateral area of the single FP. The entropy related work of the process of forming a cluster containing n_{clust} FPs is:

$$E_{ent} = N \ln\left(\frac{1}{x_0}\right) - \frac{N}{n_{clust}} \log\left(\frac{n_{clust}}{x_0}\right) \tag{S2}$$

where x_0 is the area concentration of the FPs in the system. The total energy difference between the system of separated FP and an ensemble of clusters containing n_{clust} FPs each equals the following:

$$\frac{\Delta E}{N} = \frac{E_{cluster} - E_{FP0} + E_{ent}}{N} = 2\pi\sqrt{\frac{a_0}{\pi n_{clust}}}\gamma - E_{FP} + \left(\ln\left(\frac{1}{x_0}\right) - \frac{1}{n_{clust}} \log\left(\frac{n_{clust}}{x_0}\right)\right) \tag{S3}$$

The clustering is favorable if this difference is negative, and unfavorable if it is positive. There are two adjustable parameters in this model: the FP concentration x_0 and cluster size n_{clust}. For large clusters (n_{clust} >> 1), eq. S3 greatly simplifies:

$$\frac{\Delta E}{N} \approx -E_{FP} + \ln\left(\frac{1}{x_0}\right) \tag{S4}$$

This leads to the simple criteria for cluster formation:

$$x_0 > e^{-E_{FP}}. \tag{S5}$$

A typical dependence of the energy difference ΔE on the FP concentration x_0 is shown in Figure S18(A). The black point indicates the exact solution of the equation ΔE = 0, while the vertical red line is the approximate solution according to eq. S4.

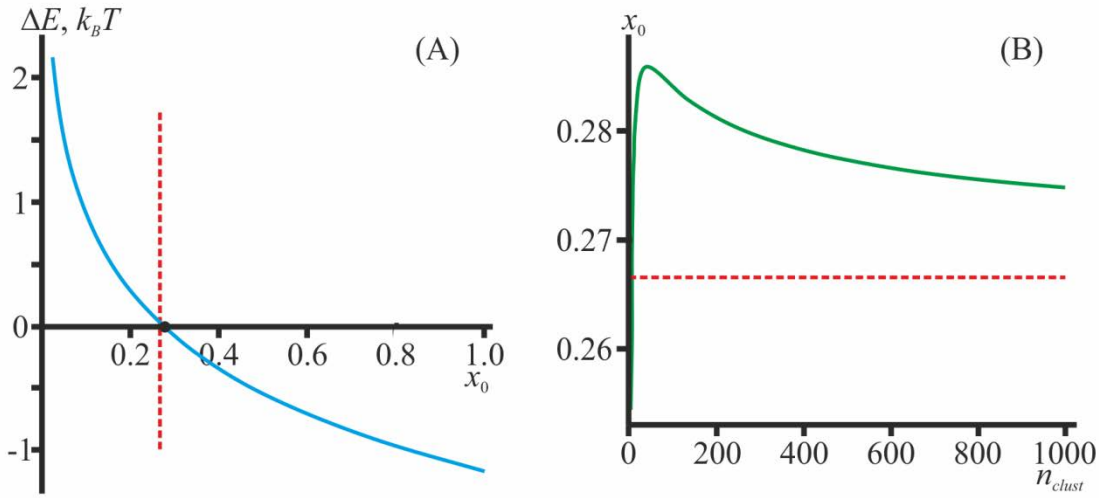

Figure S18. (A) — Dependence of the energy difference ΔE on the FP concentration x_0. The black point indicates the exact solution of the equation $\Delta E = 0$, while the vertical dashed red line is the approximate solution according to eq. S4. FP area a_0 = 3 nm^2, cluster size n_{clust} = 10, isolated FP energy $E_{FP} = 1.3\ k_BT$ = 0.8 kcal/mol, line tension of the large FP cluster $\gamma_\infty = 0.2\ k_BT$/nm = 0.8 pN. (B) — The dependence of the critical FP concentration x_0 on the cluster size. Horizontal dashed red line corresponds to the approximate solution according to eq. S4.

Since the dependence of the critical FP concentration x_0 on the cluster size appears to be very weak (Figure S18(B)), eq. S5 gives a very good estimation of the critical concentration. Eq. S3 allows analysis of the optimal cluster size. Figure S19 presents the dependence of the cluster formation energy on the cluster size for the super optimal FP concentration x_0 = 0.3. There is a clear energy minimum at the cluster size ~10. Note that this minimum is local, and at much higher sizes the energy again decreases with cluster size (Figure S19).

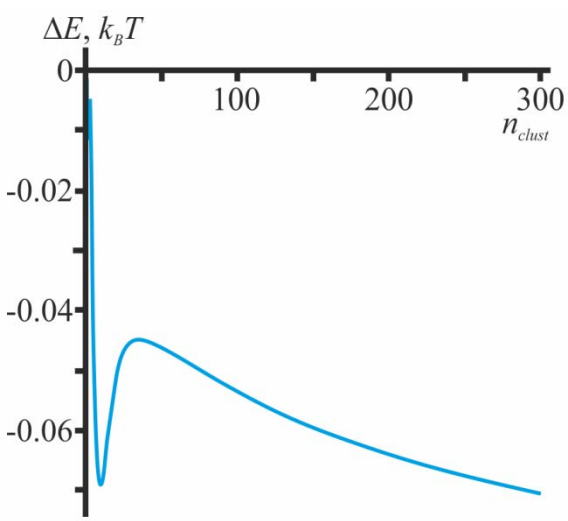

Figure S19. The dependence of the cluster formation energy on the cluster size.

Formation of hydrophobic defect in the cluster

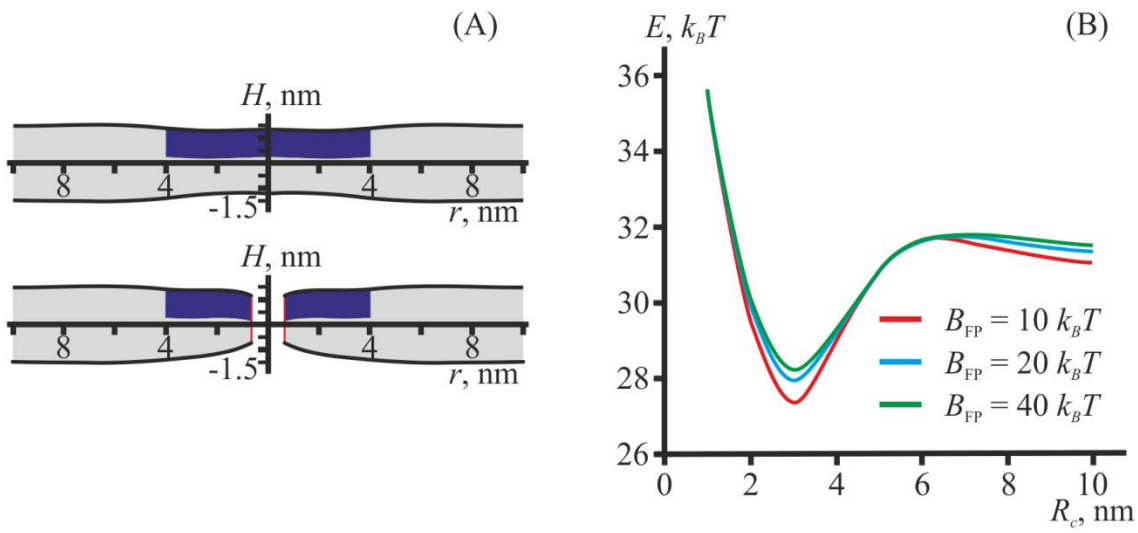

Figure S20. (A) The shape of the membrane with FP cluster in the upper monolayer without (top) and with (bottom) a hydrophobic defect in the center. The cluster is shown in blue and the lipid membrane in grey. The walls of the hydrophobic cylinder are marked by red lines. (B) The energy of hydrophobic defect formation in the center of the FP cluster as a function of the cluster radius, R_c, for different bending rigidities of the cluster monolayer, B_{FP}.

References

1 Corry, B., Jayatilaka, D., Martinac, B. & Rigby, P. Determination of the Orientational Distribution and Orientation Factor for Transfer between Membrane-Bound Fluorophores using a Confocal Microscope. *Biophysical journal* **91**, 1032-1045, doi:https://doi.org/10.1529/biophysj.106.080713 (2006).

2 Timr, Š. *et al.* Accurate Determination of the Orientational Distribution of a Fluorescent Molecule in a Phospholipid Membrane. *The Journal of Physical Chemistry B* **118**, 855-863, doi:10.1021/jp4067026 (2014).

3 Reeve, James E. *et al.* Probing the Orientational Distribution of Dyes in Membranes through Multiphoton Microscopy. *Biophysical journal* **103**, 907-917, doi:https://doi.org/10.1016/j.bpj.2012.08.003 (2012).

4 Coles, S. *An introduction to statistical modeling of extreme values*. (2011).